ALMA FIR View of Ultra High-redshift Galaxy Candidates at $z \sim$ 11-17: Blue Monsters or Low-z Red Interlopers?

Seiji Fujimoto, Steven L. Finkelstein, Denis Burgarella, Chris L. Carilli, Veronique Buat, Caitlin M. Casey, Laure Ciesla, Sandro Tacchella, Jorge A. Zavala, Gabriel Brammer, et al.

The Astrophysical Journal, 955:130 (21pp), 2023 October 1 https://doi.org/10.3847/1538-4357/aceb67

ALMA FIR View of Ultra-high-redshift Galaxy Candidates at $z \sim 11$–17: Blue Monsters or Low-z Red Interlopers?

Seiji Fujimoto[1,2,3,38], Steven L. Finkelstein[1], Denis Burgarella[4], Chris L. Carilli[5], Véronique Buat[4], Caitlin M. Casey[1], Laure Ciesla[4], Sandro Tacchella[6,7], Jorge A. Zavala[8], Gabriel Brammer[2,3], Yoshinobu Fudamoto[9,10], Masami Ouchi[8,11,12], Francesco Valentino[2,3,13], M. C. Cooper[14], Mark Dickinson[15], Maximilien Franco[1], Mauro Giavalisco[16], Taylor A. Hutchison[17,39], Jeyhan S. Kartaltepe[18], Anton M. Koekemoer[19], Takashi Kojima[11], Rebecca L. Larson[1,37], E. J. Murphy[20], Casey Papovich[21,22], Pablo G. Pérez-González[23], Rachel S. Somerville[24], Ilsang Yoon[20], Stephen M. Wilkins[25,26], Hollis Akins[1], Ricardo O. Amorín[27,28], Pablo Arrabal Haro[15], Micaela B. Bagley[1], Katherine Chworowsky[1], Nikko J. Cleri[21,22], Olivia R. Cooper[1], Luca Costantin[29], Emanuele Daddi[30], Henry C. Ferguson[31], Norman A. Grogin[19], E. F. Jiménez-Andrade[32], Stéphanie Juneau[33], Allison Kirkpatrick[34], Dale D. Kocevski[35], Aurélien Le Bail[30], Arianna Long[1,38], Ray A. Lucas[19], Benjamin Magnelli[30], Jed McKinney[1], Caitlin Rose[18], Lise-Marie Seillé[4], Raymond C. Simons[19], Benjamin J. Weiner[36], and L. Y. Aaron Yung[17,39]

[1] Department of Astronomy, The University of Texas at Austin, 2515 Speedway Boulevard Stop C1400, Austin, TX 78712-1205, USA; fujimoto@utexas.edu
[2] Cosmic Dawn Center (DAWN), Jagtvej 128, DK-2200 Copenhagen N, Denmark
[3] Niels Bohr Institute, University of Copenhagen, Lyngbyvej 2, DK-2100 Copenhagen Ø, Denmark
[4] Aix Marseille Univ, CNRS, CNES, LAM Marseille, France
[5] National Radio Astronomy Observatory, P.O. Box O, Socorro, NM 87801, USA
[6] Kavli Institute for Cosmology, University of Cambridge, Madingley Road, Cambridge, CB3 0HA, UK
[7] Cavendish Laboratory, University of Cambridge, 19 JJ Thomson Avenue, Cambridge, CB3 0HE, UK
[8] National Astronomical Observatory of Japan, 2-21-1 Osawa, Mitaka, Tokyo 181-8588, Japan
[9] Waseda Research Institute for Science and Engineering, Faculty of Science and Engineering, Waseda University, 3-4-1 Okubo, Shinjuku, Tokyo 169-8555, Japan
[10] National Astronomical Observatory of Japan, 2-21-1, Osawa, Mitaka, Tokyo, Japan
[11] Institute for Cosmic Ray Research, The University of Tokyo, 5-1-5 Kashiwanoha, Kashiwa, Chiba 277-8582, Japan
[12] Kavli Institute for the Physics and Mathematics of the Universe (WPI), University of Tokyo, Kashiwa, Chiba 277-8583, Japan
[13] European Southern Observatory, Karl-Schwarzschild-Str. 2, D-85748, Garching, Germany
[14] Department of Physics & Astronomy, University of California, Irvine, 4129 Reines Hall, Irvine, CA 92697, USA
[15] NSF's National Optical-Infrared Astronomy Research Laboratory, 950 N. Cherry Avenue, Tucson, AZ 85719, USA
[16] University of Massachusetts Amherst, 710 North Pleasant Street, Amherst, MA 01003-9305, USA
[17] Astrophysics Science Division, NASA Goddard Space Flight Center, 8800 Greenbelt Road, Greenbelt, MD 20771, USA
[18] Laboratory for Multiwavelength Astrophysics, School of Physics and Astronomy, Rochester Institute of Technology, 84 Lomb Memorial Drive, Rochester, NY 14623, USA
[19] Space Telescope Science Institute, 3700 San Martin Drive, Baltimore, MD 21218, USA
[20] National Radio Astronomy Observatory, 520 Edgemont Road, Charlottesville, VA 22903, USA
[21] Department of Physics and Astronomy, Texas A&M University, College Station, TX 77843-4242, USA
[22] George P. and Cynthia Woods Mitchell Institute for Fundamental Physics and Astronomy, Texas A&M University, College Station, TX 77843-4242, USA
[23] Centro de Astrobiología (CAB/CSIC-INTA), Ctra. de Ajalvir km 4, Torrejón de Ardoz, E-28850, Madrid, Spain
[24] Center for Computational Astrophysics, Flatiron Institute, 162 5th Avenue, New York, NY 10010, USA
[25] Astronomy Centre, University of Sussex, Falmer, Brighton, BN1 9QH, UK
[26] Institute of Space Sciences and Astronomy, University of Malta, Msida MSD 2080, Malta
[27] Instituto de Investigación Multidisciplinar en Ciencia y Tecnología, Universidad de La Serena, Raul Bitrán 1305, La Serena 2204000, Chile
[28] Departamento de Astronomía, Universidad de La Serena, Av. Juan Cisternas 1200 Norte, La Serena 1720236, Chile
[29] Centro de Astrobiología (CSIC-INTA), Ctra de Ajalvir km 4, Torrejón de Ardoz, E-28850, Madrid, Spain
[30] Université Paris-Saclay, Université Paris Cité, CEA, CNRS, AIM, F-91191, Gif-sur-Yvette, France
[31] Space Telescope Science Institute, Baltimore, MD 21218, USA
[32] Instituto de Radioastronomía y Astrofísica, UNAM Campus Morelia, Apartado postal 3-72, 58090 Morelia, Michoacán, México
[33] NSF's NOIRLab, 950 N. Cherry Avenue, Tucson, AZ 85719, USA
[34] Department of Physics and Astronomy, University of Kansas, Lawrence, KS 66045, USA
[35] Department of Physics and Astronomy, Colby College, Waterville, ME 04901, USA
[36] MMT/Steward Observatory, University of Arizona, 933 N. Cherry Street, Tucson, AZ 85721, USA
Received 2022 November 7; revised 2023 July 20; accepted 2023 July 25; published 2023 September 26

Abstract

We present Atacama Large Millimeter/submillimeter Array (ALMA) Band 7 observations of a remarkably bright galaxy candidate at $z_{\rm phot} = 16.7^{+1.9}_{-0.3}$ ($M_{\rm UV} = -21.6$), S5-z17-1, identified in James Webb Space Telescope (JWST) Early Release Observation data of Stephen's Quintet. We do not detect the dust continuum at 866 μm, ruling out

[37] NSF Graduate Fellow.
[38] Hubble Fellow.
[39] NASA Postdoctoral Fellow.

the possibility that S5-z17-1 is a low-z dusty starburst with a star formation rate of $\gtrsim$30 $M_{\odot}$ yr^{-1}. We detect a 5.1σ line feature at 338.726 $\pm$ 0.007 GHz exactly coinciding with the JWST source position, with a 2% likelihood of the signal being spurious. The most likely line identification would be [O III]52 μm at z = 16.01 or [C II]158 μm at z = 4.61, whose line luminosities do not violate the nondetection of the dust continuum in both cases. Together with three other $z \gtrsim$ 11–13 candidate galaxies recently observed with ALMA, we conduct a joint ALMA and JWST spectral energy distribution (SED) analysis and find that the high-z solution at $z \sim$ 11–17 is favored in every candidate as a very blue (UV continuum slope of $\simeq -2.3$) and luminous ($M_{\rm UV} \simeq [-24{:}-21]$) system. Still, we find in several candidates that reasonable SED fits ($\Delta\chi^2 \lesssim 4$) are reproduced by type II quasar and/or quiescent galaxy templates with strong emission lines at $z \sim$ 3–5, where such populations predicted from their luminosity functions and EW([O III]+Hβ) distributions are abundant in survey volumes used for the identification of the $z \sim$ 11–17 candidates. While these recent ALMA observation results have strengthened the likelihood of the high-z solutions, lower-z possibilities are not completely ruled out in several of the $z \sim$ 11–17 candidates, indicating the need to consider the relative surface densities of the lower-z contaminants in the ultra-high-z galaxy search.

Unified Astronomy Thesaurus concepts: High-redshift galaxies (734); Galaxy formation (595); Galaxy evolution (594)

1. Introduction

One of the major goals in modern astronomy is to understand when and how the first stars, black holes, and galaxies emerged in the Universe. Despite the effort of exploring high redshifts at $z > 10$—the first few hundred million years in our history of the Universe—only a single galaxy has been spectroscopically confirmed (GN-z11 at $z \simeq 11$; Oesch et al. 2016; Jiang et al. 2021). Because characterizing this first of stars and galaxies would bring a unique knowledge on the very first stellar populations and their impact on the early phases of galaxy evolution, and on the reionization, pushing this redshift frontier to the brink of the Big Bang and revealing the objects in the very first generations is a key driver of observational cosmology.

From its first few weeks of science operations and months by now, James Webb Space Telescope (JWST) has sparked a revolution of the effort to discover and study galaxies at very early cosmic epochs. Three early JWST observing programs have been carried out, the data of which was immediately made public: Early Release Observations (ERO; Pontoppidan et al. 2022; PID 2736) for the gravitational lens galaxy cluster SMACS J0723.3-7327 and Stephan's quintet field, and two Director's Discretionary Early Release Science (DD-ERS) programs: GLASS-JWST (PID 1324) and CEERS (PID 1345). All three programs include NIRCam imaging through multiple filters from 1–5 μm, suitable for identification of candidates for very-high-redshift objects using photometric redshifts and/or multicolor selection criteria (e.g., Adams et al. 2023; Atek et al. 2023; Bouwens et al. 2023; Castellano et al. 2022; Donnan et al. 2023; Finkelstein et al. 2022; Harikane et al. 2023b; Labbe et al. 2023; Morishita & Stiavelli 2023; Naidu et al. 2022b; Yan et al. 2023). Discounted initial zero-point calibration issues, their number, and brightness are surprising and considerably exceed most pre-JWST predictions (e.g., Ferrara et al. 2023; Mason et al. 2023; Finkelstein et al. 2023). These results indicate either the early Universe was more prolific at forming galaxies than modern simulations predict with a potential strong implication on galaxy formation models (e.g., Finkelstein et al. 2023), or there is significant foreground contamination in these early JWST high-z samples.

In this context, two of the most unique, highest-z candidates are CEERS-93316 and S5-z17-1 identified in the CEERS and Stephan's Quintet fields, respectively (Donnan et al. 2023; Harikane et al. 2023b). These candidates exhibit a clear "dropout" color signature and blue continuum slopes in NIRCam filters, interpreted as the redshifted Lyα break at $z \simeq 17$ in both sources. These candidates are securely detected in the NIRCam filters at $>10\sigma$ levels with remarkably bright ultraviolet (UV) magnitudes of 26.3 mag and 26.6 mag (AB), corresponding to the absolute UV magnitudes of ~ -22 at $z = 17$. In addition to the DSFG population, Naidu et al. (2022a) argued that similar NIRCam photometry is also reproduced by the active galactic nuclei (AGNs) in quiescent galaxies (QGs) at $z \sim 5$, with an additional environmental evidence: all three of the galaxy's nearest neighbors at $<2\farcs5$ have photometric redshifts of $z \sim 5$, and the object could lie in a $z \sim 5$ galaxy overdensity that is $\sim 5\times$ overdense compared to the field.

Recent Atacama Large Millimeter/submillimeter Array (ALMA) observations have detected millimeter emission from a significant population of "H-dropout" galaxies, undetected in Hubble Space Telescope (HST) WFC3-IR imaging, with the dropout feature even by >3 mag between HST/F160W and Spitzer/IRAC ch1 (e.g., Wang et al. 2019). These galaxies are most likely massive DSFGs at $z \sim$ 3–5 (e.g., Fujimoto et al. 2016; Franco et al. 2018; Wang et al. 2019; Williams et al. 2019; Yamaguchi et al. 2019; Sun et al. 2021; Barrufet et al. 2023; Pérez-González et al. 2023; Rodighiero et al. 2023). Moreover, these optical and near-infrared (NIR) faint DSFGs have been routinely identified in a serendipitous manner, originally targeting nearby massive galaxies (e.g., Romano et al. 2020; Fudamoto et al. 2021; Fujimoto et al. 2022). This implies that the presence of the optical-NIR faint DSFGs traces the massive dark matter halos in the early Universe (e.g., Wang et al. 2019; Zhou et al. 2020). Therefore, the tentative SCUBA2 detection and the potential overdensity environment are in line with the properties of the $z \sim$ 3–5 DSFGs recently identified in the H-dropout objects. Before concluding that CEERS-93316 and S5-z17-1 are remarkably bright $z \sim 17$ galaxies, it is essential to rule out or confirm the lower-z solution via further observations.

In this paper, we present ALMA Band 7 DDT follow-up for S5-z17-1, which is one of these remarkably UV-bright $z \sim 17$ candidates discovered in JWST ERO data of Stephan's Quintet. This is the first far-IR (FIR) characterization of either of these $z \sim 17$ candidates with ALMA,[40] setting the benchmark to understand and interpret similarly high-z candidates identified

[40] CEERS-93316 is too far north to be accessible by ALMA and has been observed in NOEMA DDT (#D22AC, PI: S. Fujimoto; see Arrabal Haro et al. 2023a).

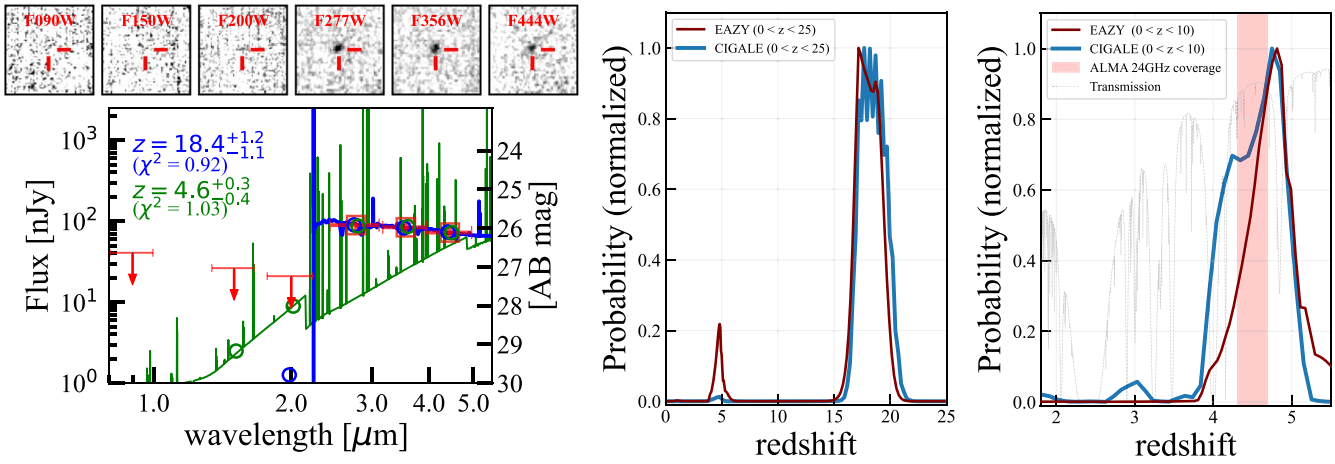

Figure 1. Left: the NIR SED of S5-z17-1. The red circles and arrows indicate the observed flux densities and 2σ upper limits, respectively. The blue and green curves and redshift labels represent the best-fit model SEDs and photometric redshifts by CIGALE with the redshift range at $0 < z < 25$ and $0 < z < 10$, respectively. The blue and green open circles are predicted flux densities in the NIRCam filters based on the best-fit SEDs. The low-z forced SED has a brighter submillimeter flux by >100 times than the best-fit high-z SED, expecting a $\sim 10\sigma$ detection from the ALMA Band 7 observation (gray curve in Figure 3). The images on this panel present $2'' \times 2''$ NIRCam cutout images of S5-z17-1. Middle: $P(z)$ from the SED fitting by EAZY (brown curve) and CIGALE (light blue curve) with a redshift range at $0 < z < 25$. Right: same as the middle panel, but at $0 < z < 10$. The gray dashed line denotes the atmospheric transmission for [C II]. The red shade indicates the [C II] redshift range of $z = 4.31$–4.69 covered by our ALMA Band 7 observations spanning 334–358 GHz with three frequency tunings, which is optimized to maximally cover the peak of the lower-redshift solution's $P(z)$ and avoid the significantly low atmospheric transmission.

in the future JWST observations. The structure of this paper is as follows. In Section 2, we describe the observations and the data reduction of both JWST and ALMA. Section 3 outlines the methods and presents the results of the continuum flux measurements, a search for any emission line, and a full spectral energy distribution (SED) analysis, including another three galaxy candidates at $z \sim 11$–13 recently observed with ALMA (GHZ1/GLz11, GHZ2/GLz13; e.g., Castellano et al. 2022; Naidu et al. 2022b; and HD1, Harikane et al. 2022). In Section 4, we discuss the physical properties of $z \sim 11$–17 candidates based on the full SED analysis results, and we also discuss the remaining low-z possibility for each candidate in Section 5. A summary of this study is presented in Section 6. Throughout this paper, we assume a flat Universe with $\Omega_m = 0.3$, $\Omega_\Lambda = 0.7$, $\sigma_8 = 0.8$, and $H_0 = 70$ km s^{-1} Mpc^{-1}, and the Chabrier initial mass function (IMF; Chabrier 2003). We place 2σ upper limits for nondetections unless otherwise specified. We take the cosmic microwave background (CMB) effect into account and correct the flux measurements at submillimeter and millimeter bands, following the recipe presented by da Cunha et al. (2013; see also e.g., Pallottini et al. 2015; Zhang et al. 2016; Lagache et al. 2018).

2. Observations and Data

2.1. JWST

Stephan's Quintet, a group of five local galaxies, was observed with NIRCam and MIRI in the JWST ERO program (Pontoppidan et al. 2022). S5-z17-1 falls in the coverage of NIRCam filters, but none of MIRI. The NIRCam images were taken in six bands: F090W, F150W, F200W, F277W, F356W, and F444W, covering 42 arcmin^2. The exposure time in each filter is ~1200 s. We use reduced and calibrated NIRCam imaging products that are publicly available,[41] and here we briefly explain the reduction and calibration procedure. The JWST pipeline calibrated level-2 NIRCam imaging products were retrieved and processed with the `grizli` pipeline (Brammer & Matharu 2021; Brammer et al. 2022) in the same manner as in Bradley et al. (2023). The NIRCam photometric zero-point correction was applied with CRDS context `jwst_0942.pmap`, including detector variations.[42] The derived photometric zero-points are consistent with those derived by other teams with a JWST ERS program (Boyer et al. 2022; Nardiello et al. 2022). While the consistent calibration results from a more recent calibration file of `jwst_0989.pmap` have been confirmed within 3% (Bradley et al. 2023), we add a potential systematic uncertainty to the flux measurement by 10% of the total flux in the following analyses to obtain secure results. The fully calibrated images in each filter were aligned with the Gaia Data Release 3 catalog (Gaia Collaboration et al. 2021), coadded, and drizzled at a 20 mas and 40 mas pixel scale for the short-wavelength (SW: F090W, F150W, F200W) and long-wavelength (LW: F277W, F356W, F444W) NIRCam bands, respectively.

2.2. ALMA

ALMA Band 7 observations were carried out on S5-z17-1 on 2022 September 16 as a Cycle 8 DDT program (#2021.A.00031.S, PI: S. Fujimoto). The requested continuum sensitivity was achieved via three frequency setups ranging nearly 24 GHz wide over ~334–358 GHz to maximize a chance of the [C II] line detection at $z = 4.31$–4.69 (red shaded region in the right panel of Figure 1), which covers around the peak of the redshift probability distribution $P(z)$ corresponding to the lower-redshift solution for S5-z17-1 due to a lower-z red galaxy with strong emission lines (Section 3.1). Each tuning was observed for 16 minutes, resulting in a total of 48 minutes including calibrations and overheads.

The ALMA data were reduced and calibrated with the Common Astronomy Software Applications package version 6.4.1.12 (CASA; THE CASA TEAM et al. 2022) with the pipeline script in the standard manner. We imaged the calibrated visibilities with natural weighting, and a pixel scale

[41] https://s3.amazonaws.com/grizli-v2/JwstMosaics/v4/index.html

[42] https://github.com/gbrammer/grizli/pull/107

Table 1
ALMA DDT Observation and Data Properties for S5-z17-1

Freq. Setup	Baseline (m)	N_{ant}	Frequency (GHz)	T_{int} (minutes)	PWV (mm)	Beam ($'' \times ''$)	$\langle\sigma_{line}\rangle$[a] ($\mu$Jy beam^{-1})	σ_{cont}[a] (μJy beam^{-1})
Tuning1	15.1–629.3	43	334.02–337.90, 346.02–349.96	5.65	0.4	0.77 × 0.46	741	78.8
Tuning2	15.1–629.3	42	338.02–341.90, 350.02–352.96	5.65	0.5	0.77 × 0.46	810	86.1
Tuning3	15.1–629.3	42	342.02–345.90, 354.02–357.96	5.65	0.4	0.77 × 0.46	759	80.7
Combined	⋯	⋯	∼334–358	16.95	⋯	0.77 × 0.46	770	45.0

Note.
[a] Standard deviation of the pixels. For the cube, we show the average value from all channels in the 60 km s^{-1} data cube.

of 0.″05. For continuum maps, the TCLEAN routines were executed down to the 2σ level with a maximum iteration number of 100,000 in the automask mode. For cubes, we adopted two common spectral channel bins of 15 and 60 km s^{-1} and applied the TCLEAN routines with the same thresholds as the continuum map. The natural and tapered maps achieved an FWHM size of the synthesized beam of 0.″77 × 0.″46 with 1σ sensitivities for the continuum and the line in a 60 km s^{-1} width channel of 45.0 μJy and 770 μJy beam^{-1}, respectively. We summarize the data properties of the continuum map and the cube in Table 1.

3. Analysis and Results

3.1. NIRCam Photometry and Redshift Solutions

We use the `grizli` photometry catalog that is also publicly available (see footnote 42). Briefly, the source fluxes in the NIRCam filters are evaluated with a circular aperture in 0.″36 diameter and corrected to MAG_AUTO. We correct the galactic dust reddening in the target direction. In the left panel of Figure 1, we present NIRCam cutouts and the `grizli` photometry for S5-z17-1. We confirm that S5-z17-1 shows a clear dropout feature between F200W and F277W filters reported in Harikane et al. (2023b), suggesting a Lyα break at $z \sim 17$. We summarize the total flux measurements of S5-z17-1 in Appendix A.

We evaluate photometric redshifts (z_{phot}) using CIGALE (Burgarella et al. 2005; Noll et al. 2009; Boquien et al. 2019). The fitting was performed in an identical fashion as in Zavala et al. (2023). In summary, we assume a delayed star formation history (SFH): SFR(t) $\propto t/\tau^2 \exp(-t/\tau)$ with stellar models from Bruzual & Charlot (2003). Dust attenuation is also added following the dust attenuation law from Calzetti et al. (2000) for the stellar continuum. The nebular emission (continuum + lines) is attenuated with a screen model and an SMC extinction curve (Pei 1992). During the SED fitting, the same $E(B-V)$ is used between stellar and nebular emission. Finally, the dust emission is reemitted in the infrared modeled with Draine et al. (2014) models. We list parameter ranges used in the fitting in Appendix C.

Figure 1 summarizes the best-fit SED (left panel) and the probability distribution function $P(z)$ (middle panel) from CIGALE. We obtain a photometric redshift of $z_{phot} = 18.4^{+1.2}_{-1.1}$, supporting that S5-z17-1 is a promising extremely high-redshift galaxy candidate (Harikane et al. 2023b). Note that Harikane et al. (2023b) reported $z_{phot} = 16.7^{+1.9}_{-0.3}$, which is slightly lower than our estimate. This is because of the faint detection ($\sim 2.4\sigma$) in the F200W filter in Harikane et al. (2023b), while our F200W photometry is below the 1σ level, probably due to the difference in the reduction and calibration of the NIRCam data and the choice of the aperture size. We confirm the general consistency of the blue continuum color in the LW filters and the photometry in all NIRCam filters between ours and the latest one of Harikane et al. (2023b; private communication) within the uncertainties.

In $P(z)$, we also identify a nonzero probability at $z \sim 5$. To assess the reasonable model for this secondary peak, we rerun CIGALE with a limited redshift range of $0 < z < 10$ and show this $P(z)$ in the right panel of Figure 1. We find that this best-fit low-redshift SED is composed of a red stellar continuum with strong rest-optical emission lines at $z_{phot} = 4.6^{+0.3}_{-0.4}$. This model also well reproduces the NIRCam photometry, including the dropout feature in the F200W band. As shown in the middle panel of Figure 1, although CIGALE suggests a much lower likelihood at $z = 4.6$ than the high-z solution based on the Bayesian approach, which applies the weights to all of the models depending on the goodness-of-fit, the difference of the χ^2 value from the high-z solution ($\Delta\chi^2 \equiv \chi^2_{highz} - \chi^2_{lowz}$) is only 0.11. This is because the optical emission lines of [O III] +Hβ and Hα+[N II] at $z \sim 4$–5 fall exactly in the F277W and F356W filters, respectively, which boosts their broadband photometric fluxes to make them resemble the Lyα break feature for very specific cases among the model parameters. This is consistent with recent arguments discussed in the other the F200W dropout object known to be a similarly promising $z \sim 17$ galaxy candidate, CEERS-93316 (Naidu et al. 2022a; Zavala et al. 2023), and such a photometry boost effect in the NIR bands due to the strong emission lines have also been demonstrated by many authors before JWST (e.g., Labbé et al. 2013; Bowler et al. 2014; Smit et al. 2014, 2015; Roberts-Borsani et al. 2016). In this forced lower-z approach, we obtain a dusty galaxy solution with SFR = 50 $M_\odot$ yr^{-1} and $M_{star} = 2.2 \times 10^8\ M_\odot$ with EW([O III]+Hβ) = 450 Å, EW(Hα+[N II]) = 240 Å, and a dust attenuation of the stellar continuum $E(B-V) = 0.47$.

We also carry out the SED fitting with EAZY (Brammer et al. 2008), which performs the SED fitting to the observed photometry with a set of templates added in a nonnegative linear combination. We use the default template set composed of the 12 `tweak_fsps_QSF_12_v3` templates derived from the Flexible Stellar Population Synthesis (FSPS) library (Conroy et al. 2009; Conroy & Gunn 2010). More details for EAZY are presented in Kokorev et al. (2022). Given our focus is to investigate the possibility that S5-z17-1 may be a lower-z red galaxy with strong emission lines suggested by CIGALE, we modify an intermediate color star-forming template of `tweak_fsps_QSF_12_v3_009` by boosting the emission line to EW([O III]+Hβ) ∼ 1100 Å in a similar manner as Labbe et al. (2023). Note that this level of high EW([O III]+Hβ) has been observed not only in young, early galaxies at $z \gtrsim 6$ (e.g., Smit et al. 2014; Endsley et al. 2021), but also in lower-z dusty

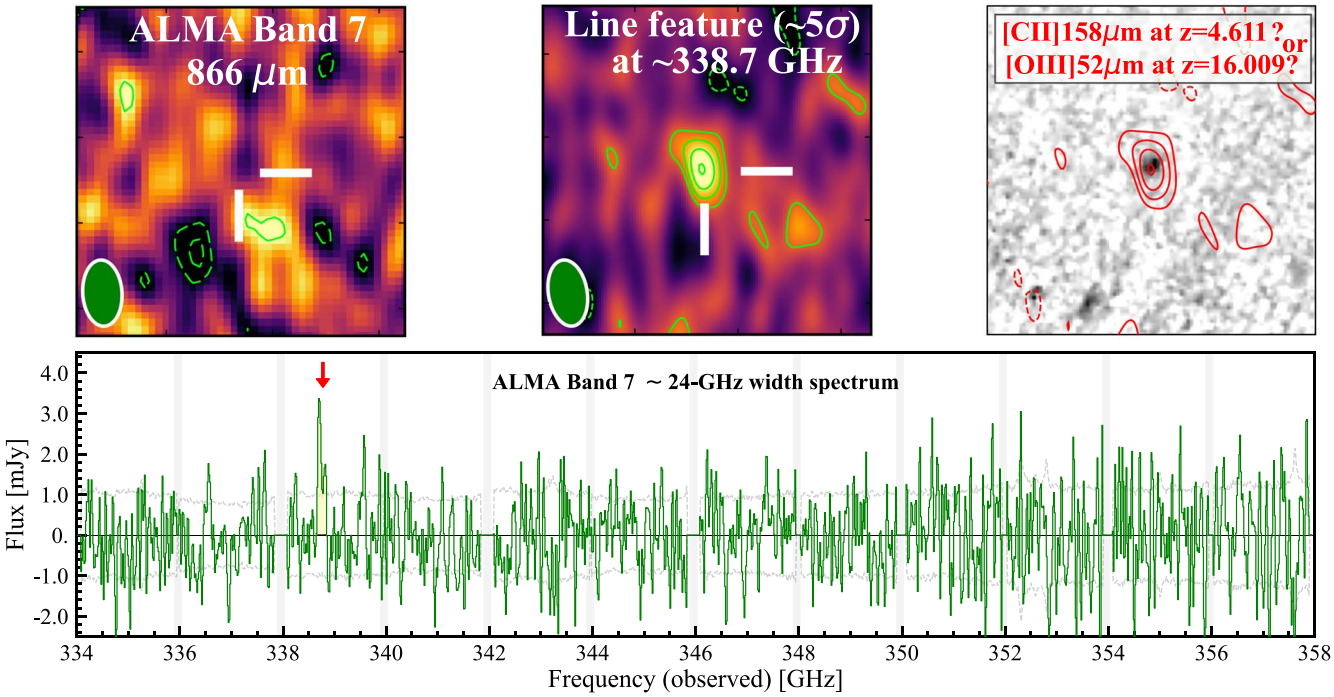

Figure 2. ALMA Band 7 observation results. Top: ALMA $4'' \times 4''$ × cutout of the continuum at 866 μm (left), the velocity-integrated map for the 5.1σ line feature at around 338.7 GHz (middle), JWST/NIRCam F356W image (right). The dashed contours indicate the -2σ and -3σ levels, while the solid contours denote the 2σ, 3σ, 4σ, and 5σ levels. The red contours overlaid on the F356W image indicate the line intensity in the moment-0 map. The green ellipse shows the ALMA synthesized beam. Bottom: ALMA ~24 GHz width spectrum (green) obtained from three frequency setups. The gray dashed line denotes the 1σ noise per channel. The gray shades show 120 MHz gaps between basedbands.

objects including quasars (e.g., Zakamska et al. 2003; Finnerty et al. 2020). We set the redshift range to span from $0 < z < 25$, in steps of 0.01. We obtain the best-fit SEDs and $P(z)$ similar to those from CIGALE in both cases: the redshift range at $0 < z < 25$ and $0 < z < 10$. Similar results are also obtained by using PROSPECTOR (Johnson et al. 2021) for CEERS-93316 (Zavala et al. 2023). The $P(z)$ from EAZY is also presented in the middle and right panels of Figure 1.

We caution that the $\Delta\chi^2$ estimate is affected by the photometry measurements including the aperture choice and the aperture correction, the definition of the photometry uncertainties, the assumed parameter spaces of the model, and the implementations of each component (e.g., stellar population synthesis, nebular emission lines) in the model among the SED fitting codes. For instance, we conservatively add a potential systematic uncertainty in the NIRCam photometry by 10% of the total flux to the original measurement uncertainty (Section 2.1), where these additional errors can easily enhance the probability of lower-z solutions (Naidu et al. 2022a). Therefore, a different $\Delta\chi^2$ estimate from previous studies does not necessary weaken the robustness of the high-z candidate selection in previous studies.

3.2. Dust Continuum and FIR Properties

The left panel of Figure 2 shows the ALMA Band 7 continuum $4'' \times 4''$ image at 866 μm. The relevant pixels show negative counts. Based on the compact source size of S5-z17-1 evaluated with NIRCam (effective radius $r_e = 0.''05$; Ono et al. 2023), we assume that the emission is unresolved with the beam ($\sim 0.''7$) in our ALMA map and place a 2σ upper limit of 90.0 μJy for the continuum emission based on the standard deviation of the map. Although we identify a weak signal ($\sim 2\sigma$) with an offset by $\sim 0.''8$, the offset is beyond the beam size, and we conclude that this nearby weak signal is a noise fluctuation irrelevant to S5-z17-1.

In Figure 3, the red arrow represents the 2σ upper limit from ALMA, and the gray curve indicates the best-fit SED at $z = 4.6$ based on NIRCam photometry with CIGALE forced at $z < 8$. The upper limit falls below the best-fit SED at $z = 4.6$, strengthening the high-z solution relative to a lower-redshift dusty galaxy with strong emission lines. We quantitatively investigate both scenarios based on the full SED analysis with the JWST and ALMA photometry in Section 3.5.

We evaluate the upper limit of the IR luminosity (L_{IR}) and obscured SFR (SFR_{IR}) for S5-z17-1 based on the following dust temperature (T_d) estimates. First, we extrapolate the best-fit redshift evolution model of T_d following the decrease of the gas depletion timescale (t_{depl}) derived in Sommovigo et al. (2022), and obtain $T_d = 90$ K at $z = 18.0$.[43] Although the extrapolation out to $z \sim 18$ is challenging, we note that t_{depl} is likely very short in S5-z17-1 due to a very compact source size of $r_e = 140^{+90}_{-60}$ pc and a very high surface SFR density of $\Sigma_{SFR} \sim 180\, M_\odot\ \mathrm{yr}^{-1}\ \mathrm{kpc}^{-2}$ from the rest-frame UV measurements with NIRCam based on the high-z solution (Ono et al. 2023).

Second, we calculate the radiative equilibrium model with a clumpy interstellar medium (ISM) distribution in the same manner as Inoue et al. (2020) and Fudamoto et al. (2023). Assuming the same rest-FIR continuum size as the F277W measurement, we obtain a lower limit of $T_d \sim 80$ K.[44] Based on

[43] We assume the gas-phase metallicity of $Z = 0.1\ Z_\odot$ and the effective dust attenuation optical depth of $\tau_{eff} = -\ln T$ with $T = 0.9$.

[44] We obtain the lower limits of 96 K and 81 K with the 2σ and 3σ upper limit of the dust continuum at 866 μm, respectively, where we adopt the lower limit of 80 K, given uncertainties from the assumptions in the model calculation.

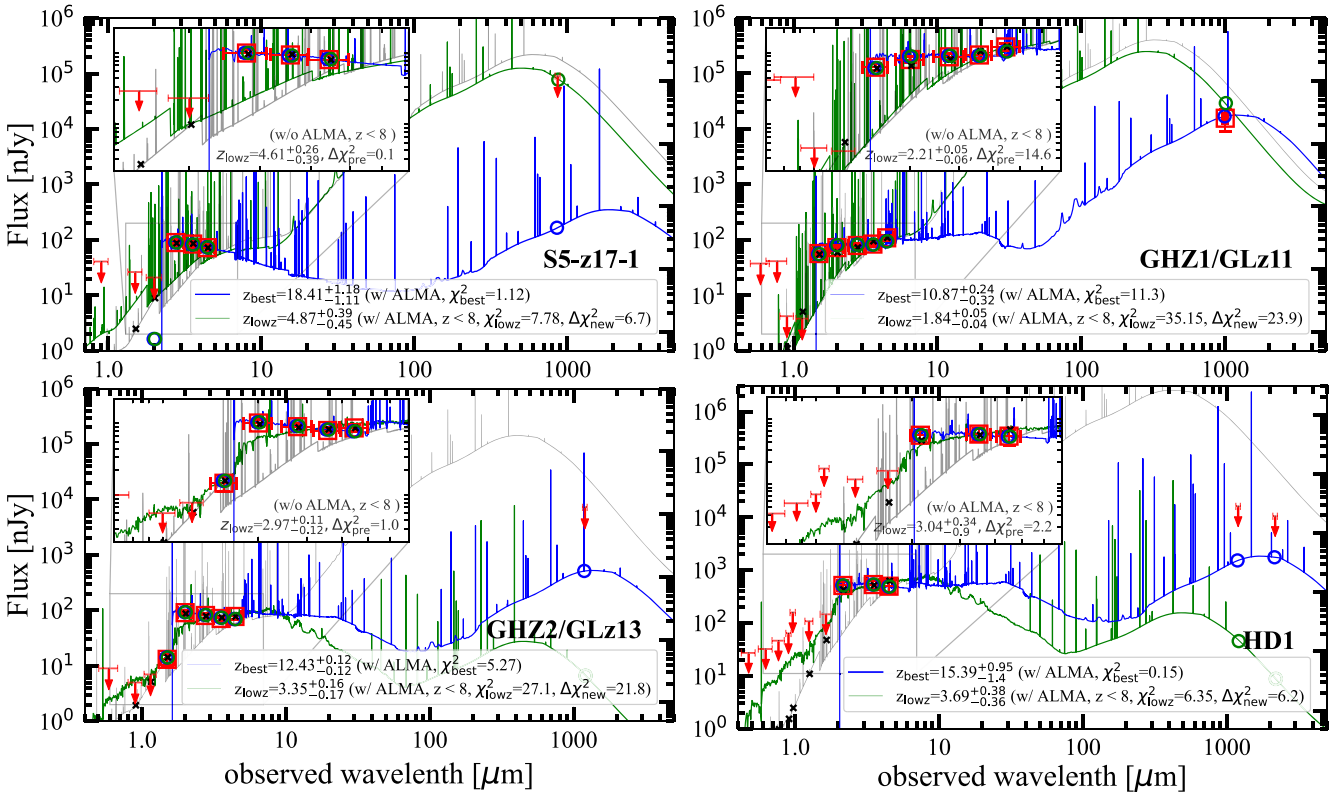

Figure 3. Optical to millimeter SED of the $z \sim 11$–17 candidates so far observed with ALMA. The red open squares and arrows indicate the observed flux densities and the 2σ upper limits, respectively. The blue curve is the best-fit SED with the optical to millimeter photometry, showing that the high-z solution is favored in all candidates. For comparison, the green and gray curves indicate the best-fit SEDs forced at $z < 8$ with and without the ALMA photometry. The lower-z IR-bright objects, implied from the gray curves, are ruled out by the new constraints from ALMA in all candidates. The $\Delta\chi^2_{\rm pre}$ and $\Delta\chi^2_{\rm new}$ values in the labels indicate the difference of the χ^2 values between the forced low-z and the best-fit high-z solutions without and with ALMA data, respectively. All candidates show $\Delta\chi^2_{\rm new}$ increased from $\Delta\chi^2_{\rm pre}$, indicating that their high-z solutions are much strengthened with the new ALMA photometry. The open circles and black crosses denote the predicted photometry from the SEDs in each filter and ALMA band.

the agreement from these two approaches, we adopt a single modified blackbody (MBB) with $T_{\rm d} = 90$ K and the dust spectral index $\beta_{\rm d} = 2.0$[45] and infer $L_{\rm IR} < 1.2 \times 10^{12}\,L_\odot$ and ${\rm SFR_{IR}} < 120\,M_\odot\ {\rm yr}^{-1}$,[46] if S5-z17-1 is truly an ultra-high-redshift object at $z \sim 18$. We caution that the CMB temperature at $z = 18$ reaches $\sim$50 K. Thus, a lower $T_{\rm d}$ assumption of, for example, 60 K also provides a similar upper limit after the CMB correction. In the case that S5-z17-1 is a lower-z object at $z \sim 4.6$ (Section 3.1), we obtain $T_{\rm d} = 49$ K from the same $T_{\rm d}(z)$ model from Sommovigo et al. (2022), which satisfies again the lower limit of $T_{\rm d} > 30$ K estimated from the radiative equilibrium model (Inoue et al. 2020; Fudamoto et al. 2023). From the same single MBB with $T_{\rm d} = 49$ K, we infer $L_{\rm IR} < 2.8 \times 10^{11}\,L_\odot$ and ${\rm SFR_{IR}} < 28\,M_\odot\ {\rm yr}^{-1}$. This rules out the possibility that S5-z17-1 is a lower-z DSFG with SFR $= 50\,M_\odot\ {\rm yr}^{-1}$, which is suggested by the forced low-z SED before ALMA (Section 3.1). We further investigate the full SED properties including the new ALMA photometry in Section 3.5. We summarize our estimates of the FIR properties in Table 2.

3.3. ALMA ∼24 GHz Width Line Scan in Band 7

To gain further insight into the redshift of this source, we analyze the ∼24 GHz wide spectrum in Band 7 to search for a serendipitous line detection. The frequency setup is optimized to cover the peak of $P(z)$ at $z = 4.31$–4.69 with [C II] 158 μm emission line and avoid the significantly low atmospheric transmission, which is summarized in the right panel of Figure 1. Note that there is a ∼120 MHz gap between each baseband. However, this frequency gap corresponds to $\sim$100 km s^{-1}, which is narrower than typical [C II] line widths of ∼300–1200 km s^{-1} among high-z DSFGs (e.g., Carilli & Walter 2013) and thus does not much affect our [C II] line identification from typical DSFGs.

In the bottom panel of Figure 2, we show the Band 7 spectrum of S5-z17-1 from the 15 km s^{-1} channel cube. Given the compact source size, we assume the emission is unresolved and extract the spectrum with a mean pixel count within a 0.″2 diameter with units of janskys per beam. In the spectrum, we identify a line feature at around 338.7 GHz, where the positive signals continue in 12 consecutive channels. We produce a velocity-integrated (moment-0) map and obtain a significance level of 5.1σ at the peak pixel in the moment-0 map. From a single Gaussian fit to the spectrum, we evaluate the line width FWHM to be 118 ± 20 km s^{-1}, a line intensity of $I_{\rm line} = 0.35 \pm 0.07$ Jy km s^{-1}, and a central frequency at 338.726 ± 0.007 GHz.

In Figure 2, we show the moment-0 map (top middle) and the contour of the line intensity overlaid on the NIRCam/F356W map (right). The peak position of the line intensity exactly matches the NIRCam source position, suggesting that

[45] This is the same assumption as Sommovigo et al. (2022) and Fudamoto et al. (2021).
[46] We assume SFR $[M_\odot\ {\rm yr}^{-1}] = 1.0 \times 10^{-10}\,L_{\rm IR}\ [L_\odot]$.

Table 2
FIR Properties of S5-z17-1

Redshift Solutions	High-z ($z \gtrsim 16$)	Lower-z ($z \sim 5$)
	Continuum	
$F_{866\ \mu m}$ (μJy)	<90.0 (2σ)	
L_{IR} ($L_\odot$)	$<1.2 \times 10^{12}$	$<2.8 \times 10^{11}$
SFR_{IR} ($M_\odot\ yr^{-1}$)	<120	<28
	Line candidate	
Classification	[O III] 52 μm	[C II] 158 μm
S/N	5.1	
Central frequency (GHz)	338.726 ± 0.007	
FWHM (km s^{-1})	118 ± 20	
I_{line} (Jy km s^{-1})	0.35 ± 0.07	
z_{line}	16.0089 ± 0.0004	4.6108 ± 0.0001
L_{line} ($L_\odot$)	$(3.8 \pm 0.7) \times 10^9$	$(2.2 \pm 0.4) \times 10^8$
SFR_{line}[a] ($M_\odot\ yr^{-1}$)	≈30–130	≈20
M_{dyn}[b] ($M_\odot$)	$\approx 1 \times 10^9$	$\approx 2 \times 10^9$

Notes.
[a] Based on SFR–L_{line} relations in De Looze et al. (2014) calibrated with local star-forming and metal-poor dwarf galaxies for the high-z and lower-z cases, respectively, where $SFR_{[O\ III]52}$ depends on the [O III]52 μm/[O III]88 μm line ratio regulated by n_e. Following the ratio of ∼1–5 ($n_e \sim 100$–$3000\ cm^{-3}$) observed in local compact H II regions (Peeters et al. 2002), we show the estimate with a range for $SFR_{[O\ III]52}$, where the lower side is comparable to the SFR estimate from the optical-mm SED fitting for the high-z solution (Table 4).
[b] Assuming an inclination angle of 45° and the diameter of $4 \times r_e$ measured with NIRCam (Ono et al. 2023).

this is one of the most promising line features among the recent ALMA observations for $z > 11$ candidates, where multiple tentative ($\sim 4\sigma$) features have been identified with small spatial offsets (Bakx et al. 2023; Harikane et al. 2022; Yoon et al. 2023). We find that other weak positive signals appeared in the spectrum (e.g., 336.6 and 339.5 GHz) always show the peak and morphology in the moment-0 map not well aligned with the NIRCam source position with spatial offsets ($\gtrsim 0\farcs2$), being the most likely noise, in contrast to the 338.7 GHz line feature. To understand the noise properties more, we also generate a data cube with a 162 km s^{-1} channel width, which consists of a total of 5,701,600 voxels based on the number of channels and the pixels of the cube. We estimate the number of similarly bright (>2 mJy) noise voxels in this data cube and find that the chance probability is estimated to be ∼2% to identify a noise peak with >2 mJy within one beam-radius search volume.

To further address the reliability of this line candidate, we also run a blind line search algorithm of FINDCLUMP implemented in a Python library of INTERFEROPY (Boogaard et al. 2021) for observational radio to millimeter interferometry data analysis.[47] For this analysis, we also produce data cubes with different channel widths of 20 km s^{-1} and 30 km s^{-1} and find that the line candidate is always recovered with signal-to-noise ratio (S/N) = 4.7–5.3 in the blind search algorithm regardless of the choice of the data cube with different channel widths. From the histograms of the positive and negative detections, the fidelity[48] at the line S/N is estimated to be ∼50%. Note that this is a blind search approach in the entire data cube. Therefore, the realistic fidelity at the source position is much higher than 50%. We conclude that the fidelity of this line candidate is (conservatively) at least 50%, and the most likely ∼98% from the above estimate based on the prior information of the target position. Given that no significant emission is detected in both continuum and each channel in the cube, we also produce the dirty cubes (i.e., applying no CLEAN) and confirm the same results. In Appendix D, we show the fidelity curve estimated from the positive and negative histograms as a function of S/N. Table 2 summarizes the properties of the line candidate.

3.4. Line Interpretation

Based on the two redshift solutions of $z_{phot} = 18.4^{+1.2}_{-1.1}$ and $z_{phot} = 4.6^{+0.3}_{-0.4}$ (Section 3.1), the possible interpretation for the line is [O III] 52 μm at $z = 16.0089 \pm 0.0004$ or [C II] 158 μm at $z = 4.6108 \pm 0.0001$. Although the middle panel of Figure 1 suggests $P(z > 16)$ is much higher than that of the lower-z solution, the F200W filter starts including the flux from the red side of the Lyα break at $z \lesssim 17$, which makes $P(z)$ at $z = 16.0$ not as high as the redshift solutions at $z \sim 17$–19. From $P(z)$, the likelihoods at $z = 16.0$ and $z = 4.6$ are almost comparable, and thus it is difficult to conclude which is more likely only from this aspect. Although the upper limit of the dust continuum rules out the possibility of the lower-z DSFG with SFR $\gtrsim 30\ M_\odot\ yr^{-1}$ (Section 3.2), we further discuss the remaining possibilities of the low-z solution in Section 5. We also explore the possibility of CO(3–2) at $z = 0.0208 \pm 0.0002$ in Appendix B, which we conclude unlikely. Therefore, we examine both interpretations in this subsection.

In the $z = 4.6$ case, we estimate a [C II] line luminosity of $L_{[C\ II]} = (2.2 \pm 0.4) \times 10^8\ L_\odot$ and SFR of $\approx 20\ M_\odot\ yr^{-1}$ based on the SFR–$L_{[C\ II]}$ relation calibrated among local star-forming galaxies (De Looze et al. 2014). This yields the $L_{[C\ II]}/L_{IR}$ ratio of $\gtrsim 8 \times 10^{-4}$, which falls in the typical range of $\sim 10^{-2}$–10^{-4} observed among dusty star-forming galaxies at $z \sim 0$–6 (e.g., Díaz-Santos et al. 2013; Gullberg et al. 2015). In the $z = 16.0$ case, we calculate an [O III] 52 μm line luminosity of $L_{[O\ III]52} = (3.8 \pm 0.7) \times 10^9\ L_\odot$. Based on the SFR–$L_{[O\ III]88}$ relation estimated among local metal-poor galaxies (De Looze et al. 2014) and the typical line ratio of [O III]52 μm and [O III] 88 μm lines of ∼1–5 observed in local compact H II regions (Peeters et al. 2002), we evaluate the SFR value to be ≈30–130 $M_\odot\ yr^{-1}$. Although systematic uncertainties remain in the application of these empirical relations, we confirm that our line-based SFR estimates are consistent with the upper limits of SFR_{IR} from the dust continuum in both cases. We caution that the high [O III]52 μm/88 μm ratio[49] of ∼5 indicates a high electron density of $n_e \sim 3000\ cm^{-3}$, which exceeds the critical density of [O III] 88 μm. It is thus unclear whether the assumed SFR–$L_{[O\ III]88}$ relation, which is also affected by the metallicity and ionization parameter, is validated in this high n_e regime. A dedicated analysis will be necessary in a separate paper.

Following the method outlined in Wang et al. (2013),[50] we also estimate a dynamical mass of $M_{dyn} \approx 2 \times 10^9 M_\odot$ and

[47] https://interferopy.readthedocs.io/en/latest/index.html
[48] Fidelity (S/N) ≡ [N(positive) − N(negative)]/N(positive), where N is the number of detection with a given S/N.
[49] The [O III]52 μm/88 μm line ratio is regulated by electron density due to difference of their critical densities, and not much affected by metallicity and ionization parameter (e.g., Jones et al. 2020; Yang et al. 2021).
[50] In approximation, the dynamical mass is given by $M_{dyn} = 1.16 \times 10^5 V_{circ} D$, where D is the diameter and V_{circ} is circular velocity. V_{circ} is also given by $V_{circ} = 1.763 \sigma_{line}/\sin(i)$, where i is inclination angle and σ_{line} is the velocity dispersion of the line. We assume an inclination of 45° and $D = 4 \times r_e$ from the NIRCam observation.

Table 3
Summary of UV Luminous $z \sim 11$–17 Galaxy Candidates Observed with ALMA

Source Name	R.A. (deg)	Decl. (deg)	$z_{\rm phot}^{\rm literature}$	F444W (mag)	$\lambda_{\rm obs}^{\rm ALMA}$ (mm)	$F_{\rm ALMA}$ (μJy)	References
(1)	(2)	(3)	(4)	(5)	(6)	(7)	(8)
S5-z17-1	339.015969	33.904624	$16.7^{+1.9}_{-0.3}$	26.75 ± 0.17	0.87	<90.0	This work
GHZ1/GLz11	3.498988	−30.324759	$10.4^{+0.2}_{-0.7}$	26.31 ± 0.11	1.21	(15.6 ± 5.8)	Y22
GHZ2/GLz13	3.511923	−30.371859	$12.4^{+0.1}_{-0.3}$	26.67 ± 0.11	1.02	<7.2	B22, P22
HD1	150.463792	2.547222	$15.2^{+1.2}_{-2.7}$	24.67 ± 0.30	1.27	<16.0	H22
					2.17	<10.4	K22

Note. (1) Source name in literature. (2) R.A. (3) Decl. (4) Photometric redshift estimate in literature (S5-z17-1: Harikane et al. 2023b, GHZ1/GLz11 and GHZ2/GLz13: Naidu et al. 2022b, HD1: Harikane et al. 2022). (5) Our total magnitude estimate in NIRCam/F444W filter with 1σ errors. The potential systematic uncertainty is added by 10%. For HD1, we show the total magnitude estimate of Spitzer IRAC ch2 in Harikane et al. (2022). (6) Observed wavelength in the ALMA observation based on the center sky frequency. (7) Submillimeter-to-millimeter photometry from our and recent ALMA observations. The upper limit is placed at the 2σ level, and a tentative 2.6σ emission is reported in GHZ1/GLz11 (Yoon et al. 2023). (8) Reference of the ALMA observation (Y22: Yoon et al. 2023, B22: Bakx et al. 2023, P22: Popping 2023, H22: Harikane et al. 2022, and K22: Kaasinen et al. 2023).

$\approx 1 \times 10^9 M_\odot$ in the $z = 4.6$ and $z = 16.0$ cases, respectively. In the $z = 4.6$ case, the $M_{\rm star}$ value is estimated to be $2 \times 10^8\, M_\odot$ in our forced low-z SED analysis (Section 3.1), and thus the $M_{\rm star}/M_{\rm dyn}$ ratio is about 10%. Also with the upper limit of $\rm SFR_{IR}$, this suggests that S5-z17-1 is a moderately star-forming, very gas-rich system (gas fraction ∼90%) at $z = 4.6$, which is consistent with the recent ALMA results for main-sequence galaxies surrounded by rich metal-rich gas reservoir at $z \sim 4$–7 (e.g., Fujimoto et al. 2019, 2020, 2021; Dessauges-Zavadsky et al. 2020). In the high-z scenario, Harikane et al. (2023b) evaluated $M_{\rm star} = 7.0^{+50.8}_{-4.8} \times 10^8\, M_\odot$ for S5-z17-1, which satisfies $M_{\rm star} \leqslant M_{\rm dyn}$. Assuming that $M_{\rm dyn}$ is dominated by the molecular gas and stellar masses, the above estimates indicate a low gas fraction (≈0.3) in the high-z scenario, which is likely consistent with the decreasing trend of the gas fraction with increasing stellar mass (e.g., Tacconi et al. 2013). Note that for the structure formation model with Planck cosmology (UNIVERSEMACHINE; Behroozi et al. 2020), the most massive dark matter halos at $z = 16.0$ are calculated to be $M_{\rm halo} \sim 8 \times 10^9\, M_\odot$. Thus, the $M_{\rm star}/M_{\rm halo}$ ratio can be still ∼0.09, which satisfies the upper boundary from the cosmic baryon fraction of 0.16. One note is that such a high stellar-to-halo-mass ratio implies a significantly high star formation efficiency. We further discuss the validity of the high-z solution in Section 4.1.

Based on these results, both interpretations are possible, and it is challenging to conclude which is more likely with the current data sets. Once the line feature is confirmed, the low-z solution at $z = 4.61$ will be verified with the JWST/NIRSpec follow-up by targeting the strong rest-frame optical emission lines that cause the dropout feature between the F200W and F277W filters. In fact, this is the case of another extremely high-z galaxy candidate, initially estimated at $z \sim 17$ (e.g., Donnan et al. 2023), which has been subsequently spectroscopically confirmed to be at $z = 4.91$ (Arrabal Haro et al. 2023a). If we do not detect any emission lines from NIRSpec, ALMA follow-up observations for the [O III] 88 μm line will be a plausible approach to spectroscopically confirm the high-z solution at $z = 16.01$, since the bright rest-frame optical emission lines (e.g., [O III]5007, Hβ) shift out of the spectral window of NIRSpec at $z \gtrsim 11$. We summarize the properties of the line candidate in both cases in Table 2.

3.5. JWST+ALMA Joint SED Analysis

The nondetection of the dust continuum from S5-z17-1 is reminiscent of recent ALMA results in other three UV-bright galaxy candidates at $z \sim 11$–13: GHZ1/GLz11, GHZ2/GLz13, and HD1 (Bakx et al. 2023; Harikane et al. 2022; Kaasinen et al. 2023; Popping 2023; Yoon et al. 2023). GHZ1/GLz11 and GHZ2/GLz13 were also identified in the early JWST data from the GLASS field (Treu et al. 2022) from different teams (e.g., Castellano et al. 2022; Donnan et al. 2023; Naidu et al. 2022b; Harikane et al. 2023b). No robust dust continuum is detected in follow-up deep 1 mm observations with a total of >10 hr observing time for both candidates (Bakx et al. 2023; Popping 2023; Yoon et al. 2023), while a tentative (2.6σ) detection is reported in GHZ1/GLz11 (Yoon et al. 2023). HD1 was found as a remarkably bright ($M_{\rm UV} \sim -24$) galaxy candidate at $z \sim 13$ in a systematic search over a 2.3 deg^2 area in ground-based telescopes and Spitzer data (Harikane et al. 2022). Similarly deep ALMA 1 and 2 mm band observations have been carried out, showing no dust continuum detection in both ALMA observations (Harikane et al. 2022; Kaasinen et al. 2023). These results may imply a low possibility of contamination from lower-z dusty star-forming galaxies with strong emission lines among the high-z candidates at $z \sim 11$–17 recently identified and observed with ALMA. In Table 3, we summarize S5-z17-1 and these three UV-bright high-z galaxy candidates so far observed with ALMA.

To further investigate the high-z ($z \gtrsim 11$) and the lower-z scenarios for all of these candidates, we perform SED fitting to the optical to millimeter photometry using CIGALE (Burgarella et al. 2005; Noll et al. 2009; Boquien et al. 2019). We adopt the same assumptions in the fitting described in Section 3.1. We use the public *grizli* catalog for GHZ1/GLz11 and GHZ2/GLz13, where the JWST data reduction, calibration, and photometry are processed in the same manner as S5-z17-1 (Section 2.1). We also use the photometry of the HST/ACS–WFC3 images in the catalog, including the latest ACS data taken as part of a DDT program (#17231, PI: T. Treu), which is processed using the `grizli` pipeline in the same manner as Kokorev et al. (2022). We list the JWST and HST photometry of GHZ1/GLz11 and GHZ2/GLz13 in Appendix A. The optical-NIR photometry of HD1 is taken from Harikane et al. (2022). The ALMA photometry measurements of GHZ1/

GLz11, GHZ2/GLz13, and HD1 are taken from the previous studies (Bakx et al. 2023; Harikane et al. 2022; Kaasinen et al. 2023; Popping 2023; Yoon et al. 2023). We use the photometry with the 1σ error also for the measurements below the 2σ upper limits. When the literature only provides the upper limit, we set zero flux with the 1σ error in those nondetection bands. To maintain the same detection thresholds among different wavelengths, we use the 2.6σ detection in the ALMA 1 mm band in GHZ1/GLz11.

In Figure 3, we show the best-fit SED (blue curve) with the optical to millimeter photometry (red symbols). For comparison, we also show the best-fit SED forced at $0 < z < 8$ with (green curve) and without the ALMA photometry (gray dashed curve). For every candidate, we find that the best-fit SED from the optical to millimeter photometry not only favors the high-z solution at $z \gtrsim 11$. Moreover, the ALMA photometry always falls below the gray dashed curve, suggesting that the possibility of lower-z IR-bright DSFGs are ruled out. Still, the possibility of lower-z, IR-faint red objects might remain, which corresponds to the best-fit SED forced at low-z with the ALMA photometry (green curves). In the inset labels, we also present the $\Delta\chi^2$ values of the forced low-z solutions from the best-fit high-z solutions in the SED analysis before ($\Delta\chi^2_{\rm pre}$) and after including the ALMA photometry ($\Delta\chi^2_{\rm new}$). We find that the $\Delta\chi^2$ value increases in every candidate out to $\sim$6–27 (i.e., $\Delta\chi^2_{\rm pre} < \Delta\chi^2_{\rm new}$; the addition of the ALMA nondetection increases the likelihood of the high-redshift solution relative to the low-redshift solution), satisfying the criterion of $\Delta\chi^2 > 4.0$, corresponding to a 2σ level, used in previous studies (e.g., Bowler et al. 2020; Donnan et al. 2023; Harikane et al. 2022; Finkelstein et al. 2023). These results suggest that the lower-z IR-faint red objects are also unlikely supported, although $\Delta\chi^2$ values may change with different SED codes and assumptions (e.g., high $T_{\rm dust}$). We further discuss the remaining possibilities of the lower-z solution in Section 5.

4. Blue Monsters at $z \sim 11$–17

4.1. Presence of UV-bright Galaxies out to z ∼ 17

Owing to our and recent deep ALMA observations, the high-z solutions at $z \sim 11$–17 are all favored in the UV-bright high-z candidates of S5-z17-1, GHZ1/GLz11, GHZ2/GLz13, and HD1 (Section 3.5). In particular, the high-z solution obtained from S5-z17-1 suggests the presence of the remarkably UV-bright ($M_{\rm UV} = -21.9$) object at $z \sim 17$, just $\sim$200 Myr after the Big Bang. This UV luminosity is comparable to that of GN-z11 (Oesch et al. 2016), making S5-z17-1 the second most luminous object at $z > 11$ after HD1 ($M_{\rm UV} = -23.6$). Such an identification in the small survey volume among the early JWST observations could present a challenge to the current models of early galaxy formation and potentially even the underlying Λ cold dark matter (CDM) cosmological framework (e.g., Steinhardt et al. 2016, 2023; Boylan-Kolchin 2022; Lovell et al. 2023; Mason et al. 2023; Menci et al. 2022). As discussed in Naidu et al. (2022a), no theoretical UV LF or empirical extrapolation can be close to matching with its presence, except for a 100% instantaneous star formation efficiency coupling with the dark matter halo-mass function, while the star formation efficiency measured at $z \sim 6$–10 is typically <10% (e.g., Finkelstein et al. 2015; Tacchella et al. 2018; Stefanon et al. 2021).

Harikane et al. (2023b) discussed three possible scenarios (see also Inayoshi et al. 2022) for the presence of a remarkably UV-bright object even out to $z \sim 17$: (A) no star formation suppression, (B) presence of AGNs, and (C) Population III like stellar population with a top-heavy IMF. For the scenario (A), recent numerical studies of star cluster formation from compact giant molecular clouds also indicate high star formation efficiency when an initial gas surface density is sufficiently high (Kim et al. 2018; Fukushima et al. 2020; Fukushima & Yajima 2021, see also Krumholz et al. 2019). In fact, assuming the Kennicutt–Schmidt relation (Kennicutt 1998) and that the spatial distributions of gas and UV-emitting regions are the same, the UV bright and compact properties of S5-z17-1 imply a high gas density of $\Sigma_{\rm gas} \simeq 1.5 \times 10^4\, M_\odot\ {\rm pc}^{-2}$ or even higher out to $\simeq 5.6 \times 10^4\, M_\odot\ {\rm pc}^{-2}$, given the current upper limit of the obscured ${\rm SFR_{IR}} < 120\, M_\odot\ {\rm yr}^{-1}$ in the high-z case (Section 3.2). If we assume these gas density estimates and assume a gas-phase metallicity of $Z = 0.01\ Z_\odot$, an analytical model developed in Fukushima & Yajima (2021) suggests the star formation efficiency to be $\simeq$0.7–1.0. Although the spec-z confirmation is essentially required, the presence of S5-z17-1 at $z \sim 17$ may not necessarily contradict with the current early galaxy evolution models and underlying ΛCDM framework, based on the observed properties so far.

4.2. Dust Poor Universe at z ≳ 11

Recent ALMA observations for UV-bright galaxies dominating the bright-end of the UV luminosity function (LF) show successful detection of the dust continuum from $\sim$40% of the sample at $z \sim 7$ (Bouwens et al. 2022; Inami et al. 2022). In contrast, we do not detect robust continuum detection from any of the $z \sim 11$–17 candidates, although they also dominate the bright-end of the UV LF at these redshifts (e.g., Donnan et al. 2023; Harikane et al. 2023b). This might imply that a transition is taking place in dust properties of early galaxies between $z \gtrsim 11$ and $z \sim 7$.

In Figure 4, we show our measurements of the infrared excess IRX ($\equiv L_{\rm IR}/L_{\rm UV}$), UV continuum slope $\beta_{\rm UV}$, and $M_{\rm star}$ for the $z \sim 11$–17 candidates. We evaluate the $L_{\rm IR}$ values with the single MBB based on the following two assumptions: the $T_{\rm d}$–z relation of Sommovigo et al. (2022), and a constant value of $T_{\rm d} = 50$ K. The other measurements are taken from the best-fit results from CIGALE summarized in Table 4. For comparison, we also present the measurements obtained in other high-z star-forming galaxies in recent ALMA large surveys of ASPECS at $z \sim 2$–3 (e.g., Bouwens et al. 2020), ALPINE at $z \sim 4$–6 (e.g., Fudamoto et al. 2020; Burgarella et al. 2022), and REBELS at $z \sim 7$ (e.g., Inami et al. 2022). We find that the UV-bright $z \sim 11$–17 candidates are generally characterized as bluer and less IR-bright systems than the REBELS galaxies, despite similar $M_{\rm star}$ values. Ziparo et al. (2023) discussed two possible scenarios for relatively massive ($M_{\rm star} \sim 10^{8-9}\, M_\odot$) and blue ($\beta_{\rm UV} < -2.0$) high-$z$ ($z > 10$) candidates identified in recent JWST observations: (a) ejected by the radiation pressure (see also Ferrara et al. 2023), or (b) segregated with respect to UV-emitting regions. Because the nondetection of the dust continuum disfavors the scenario (b), the massive and blue properties observed in the $z \sim 11$–17 candidates likely support scenario (a).

We note that not all of the upper limits of IRX in the $z \sim 11$–17 candidates are similarly deep as the lowest IRX regime observed in the ALPINE and REBELS results. Thus,

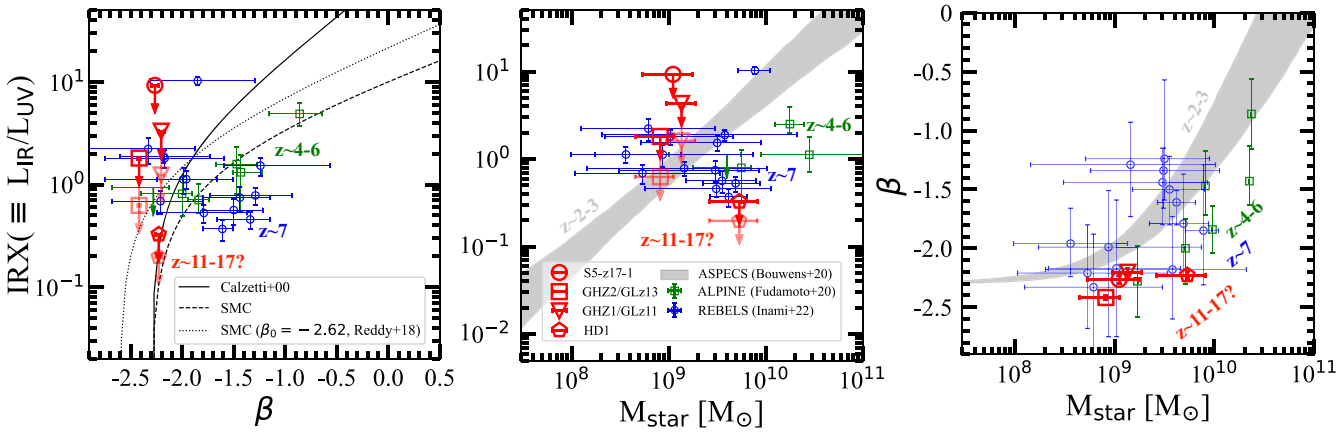

Figure 4. Comparison of IRX, $\beta_{\rm UV}$, and $M_{\rm star}$ properties with other high-z star-forming galaxies constrained from recent large ALMA surveys of ASPECS at $z\sim2$–3 (Walter et al. 2016), ALPINE at $z\sim4$–6 (green square; Le Fèvre et al. 2020), and REBELS $z\sim7$ (blue square; Bouwens et al. 2022). Note that ASPECS and ALPINE results are taken from the stacking results (Bouwens et al. 2020; Fudamoto et al. 2020), while REBELS results are taken from the individual results based on detection (e.g., Inami et al. 2022; Sommovigo et al. 2022). The red symbols represent the UV-bright ($M_{\rm UV}\approx[-24:-21]$) high-$z$ candidates at $z\sim11$–17 constrained from our optical to millimeter SED analysis. The solid and light red symbols are estimated from the $T_{\rm d}$–z relation of Sommovigo et al. (2022) and a constant assumption of $T_{\rm d}=50$ K, respectively. The upper limits are placed at the 2σ level, while we place the 2.6σ upper limit for GHZ1/GLz11 that has been reported to have a tentative (2.6σ) continuum emission (Yoon et al. 2023). Left: IRX–$\beta_{\rm UV}$ relation. The solid and dashed curves indicate the relations derived with the dust attenuation of SMC and Calzetti et al. (2000), respectively. The dotted curve shows the relation derived with the SMC dust attenuation and bluer intrinsic $\beta_{\rm UV}$. Middle and right: IRX–$M_{\rm star}$ and $M_{\rm star}$–$\beta_{\rm UV}$ relations from middle to right. The black shade shows the 1σ range of the best-fit relations at $z\sim2$–3 estimated in Bouwens et al. (2020). Although both UV-bright $z\sim11$–17 candidates and the REBELS sources dominate the bright-end of the UV LF and the similar $M_{\rm star}$ range at these redshifts, the former is generally bluer and lower IRX.

Table 4
Physical Properties of $z=11$–17 Candidates from Optical to Millimeter SED Fitting

Source Name	$z_{\rm best}$ (χ^2)	$z_{\rm lowz}$ (χ^2)	$\Delta\chi^2$	$M_{\rm UV}$ (mag)	$\beta_{\rm UV}$	SFR$_{\rm 10Myr}$ ($M_\odot$ yr^{-1})	$M_{\rm star}$ ($10^9\,M_\odot$)
	(1)	(2)	(3)	(4)	(5)	(6)	(7)
S5-z17-1	$18.41^{+1.18}_{-1.11}$ (1.12)	$4.45^{+0.46}_{-0.52}$ (7.84)	6.71	-21.87 ± 0.11	-2.04 ± 0.05	23^{+8}_{-4}	$1.1^{+0.7}_{-0.6}$
GHZ1/GLz11	$10.87^{+0.24}_{-0.32}$ (11.3[a])	$1.84^{+0.05}_{-0.04}$(35.15)	23.85	-21.03 ± 0.12	-2.29 ± 0.02	15^{+3}_{-2}	$1.4^{+0.5}_{-0.4}$
GHZ2/GLz13	$12.43^{+0.12}_{-0.12}$ (5.27[a])	$3.35^{+0.16}_{-0.17}$(27.10)	21.83	-21.35 ± 0.07	-2.45 ± 0.01	13^{+2}_{-1}	$0.8^{+0.3}_{-0.4}$
HD1	$15.39^{+0.95}_{-1.40}$ (0.15)	$3.69^{+0.38}_{-0.36}$(6.35)	6.20	-23.64 ± 0.18	-2.22 ± 0.03	101^{+24}_{-16}	$5.4^{+2.8}_{-2.7}$

Notes. (1) Photometric redshift with the best-fit SED at $0<z<25$. The χ^2 value is shown in parentheses. (2) Photometric redshift with the best-fit SED forced at $0<z<8$. The χ^2 ($z_{\rm lowz}$) value is shown in parentheses. (3) Difference of the χ^2 values between the best-fit SEDs at $z_{\rm best}$ and $z_{\rm lowz}$. (4)–(7) Physical properties in the high-z solutions based on $z_{\rm best}$: (4) Absolute UV magnitude, (5) UV continuum slope measured by a single power-low fit to the continuum component in the best-fit SED over rest-frame 1400–2500 Å in a similar manner as Nanayakkara et al. (2023), (6) Average SFR over 10 Myr, (7) Stellar mass.
[a] The best-fit SEDs with smaller χ^2 values are obtained in the literature, while our measurements include the new ALMA photometry, which affects the best-fit parameter space and the χ^2 value.

there is a possibility that these $z\sim11$–17 candidates also follow the IRX relations similar to the $z\sim2$–7 galaxies, while the upper limits of ALMA might be still insufficient to capture the dust emission from them. Nevertheless, the parameter space currently constrained by HD1 already explores the most massive, bluest, and IR-faintest regimes, which deviate from the relations evaluated by stacking for ASPECS and ALPINE sources at $z\sim2$–6. In addition to its very massive ($M_{\rm star}\sim10^{10}\,M_\odot$) aspect at $z\sim13$ in the ΛCDM framework (e.g., Steinhardt et al. 2016, 2023; Boylan-Kolchin 2022; Lovell et al. 2023; Mason et al. 2023; Menci et al. 2022), HD1 will be the most challenging object also with respect to dust properties, once the redshift is spectroscopically confirmed.

5. Other Potential Low-z Interlopers

Along with the discussions in Zavala et al. (2023) and Naidu et al. (2022a), our initial SED analysis confirms that lower-z line-emitting red objects can reproduce clear dropout features in the NIR filters, which resembles the Lyα break feature from very high-z galaxies (Section 3.1). Although we rule out the possibility of lower-z DSFGs with SFR of $>30\,M_\odot$ yr^{-1} for S5-z17-1 and similar constraints obtained in the other three candidates, owing to the deep constraints on dust continuum emission from our and recent ALMA observations (Section 3.5), caution is still required given the presence of populations other than DSFGs that might also play a part of the line-emitting red continuum objects, such as dusty quasars (QSOs) and AGNs emerged in QGs (see also discussion in Naidu et al. 2022a). In particular, more caution may be required when the objects are remarkably luminous and at high redshift, where the abundance can be overwhelmed by rare populations at lower redshifts. Note that all of the candidates at $z\sim11$–17 studied in this paper, except for HD1, which was originally identified from ground-based telescopes and Spitzer, have been observed with spatially resolved morphology in the superb resolution of JWST/NIRCam images (e.g., Ono et al. 2023; Yang et al. 2022). The spatially resolved morphology suggests that these candidates are unlikely type I QSOs with a point-

source morphology. However, there still remains a possibility of type II QSOs or very faint type I QSOs, where the contrast of the host galaxy to the central QSO becomes high. Given these potential contributions from lower-z rare objects, we investigate the remaining lower-z possibility from three aspects: (i) EW distribution of the optical emission lines, (ii) optical to millimeter SED properties, and (iii) abundance in the following subsections. Given the requirement of the red continuum and strong emission lines for the lower-z interlopers to make the NIR dropout feature, we focus on the following two populations: type II and/or dusty type I QSOs/AGNs, and QGs harboring AGNs (QG+AGN).

5.1. Distribution of EW([O III]+Hβ)

First, we examine the distributions of EW([O III]+Hβ) for type II/dusty type I QSO and QG+AGN populations that might contribute to the NIR dropout objects. Note that the emission lines of ionized gas have been identified in QGs likely due to AGNs (e.g., Belli et al. 2017b, 2019; Ito et al. 2022; Kubo et al. 2022). In the optical-to-NIR SED analysis forced to the lower-z solution (Section 3.1), we find that a dusty galaxy with EW([O III]+Hβ) = 450 Å reproduces the F200W dropout feature of S5-z17-1. In the same analysis for GHZ1/GLz11, GHZ/GLz13, and HD1, we obtain an EW range of EW([O III] +Hβ) = 140–490 Å from the best-fit SEDs forced at lower-z. Because more robust dropout features can be produced with higher EW values, we regard the range of EW([O III] +Hβ) = 140–490 Å as the minimum required EW values for the lower-z interlopers to contaminate the high-z candidates ($z \gtrsim 11$) in the following analysis.

In Figure 5, we show the distributions of EW([O III]+Hβ) for type II / dusty type I QSO[51] and QG+AGN populations (Zakamska et al. 2003; Finnerty et al. 2020; Forrest et al. 2020).[52] For comparison, we also show the minimum required EW values for the lower-z interlopers (gray shade). Based on the distribution and the lower bound of the gray shade, we find that ∼40% (∼100%) of the type II QSOs (dusty type I QSOs) fall in and above the minimum required EW range and that the maximum EW([O III]+Hβ) value reaches ∼3000 Å (∼9000 Å). We also find that the QG+AGN population has the EW([O III] +Hβ) distribution out to ∼300 Å, where ∼40% of them fall in and above the minimum required EW range. Because about 10% of the QGs at high redshift harbor emission lines that are likely powered by the AGN (e.g., Belli et al. 2017a, 2019), we estimate ∼4% (=0.1 × 0.4) of the QGs satisfy the minimum required EW range. By stacking Keck/NIRES spectra, an average EW of the hot obscured dusty objects at $z \sim 1$–4 is also estimated to be ∼400 Å (McKinney et al. 2023). These results indicate that subsets of QSO and QG populations may actually be included in the high-z ($z \gtrsim 11$) candidates by contributing to the NIR dropout feature with the red continuum and strong emission lines.

5.2. Optical-to-millimeter SED Analysis

Second, we examine the optical-to-millimeter SED properties with the following two populations in this subsection: (1) type II QSOs and (2) QG+AGN. Based on the EW([O III]+Hβ) distribution of each population in Figure 5, we assume EW([O III]+Hβ) = 1000 Å and 300 Å for the type II QSO and the QG+AGN populations, respectively, by boosting the key optical emission lines of [O III]4959, 5007, Hβ, Hα, and [N II] in the type II QSO and QG templates taken from Polletta et al. (2006, 2007). We follow the line ratios of the most highly ionized system in Richardson et al. (2014).

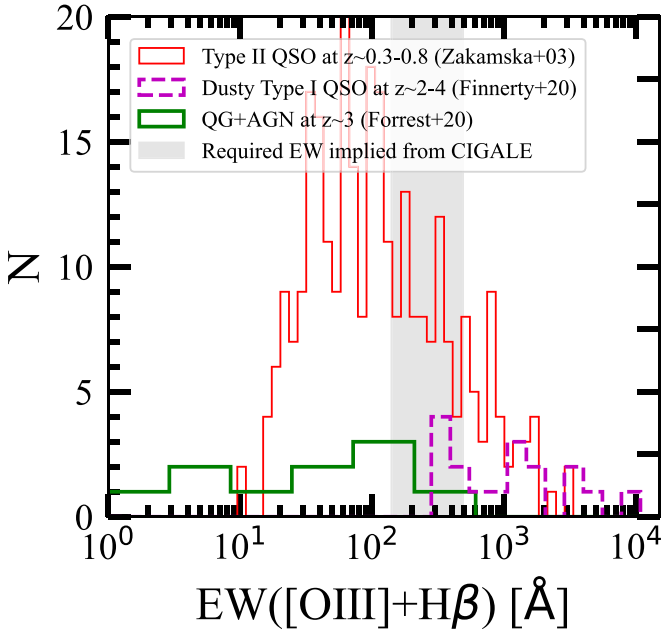

Figure 5. Distribution of the rest-frame EW([O III]+Hβ) for several quasar and galaxy populations that might attribute to the $z \sim 11$–17 candidates: type II QSOs (Zakamska et al. 2003), dusty-reddened type I QSOs (Finnerty et al. 2020), and QGs with emission lines from AGNs (Forrest et al. 2020). The gray shaded region indicates the required EW([O III]+Hβ) range implied from the CIGALE modeling, showing the minimum to maximum range among the best-fit SEDs of S5-z17-1, GHZ1/GLz13, GHZ2/GLz11, and HD1 forced at $z < 8$. When the literature does not show the Hβ line measurement, we include the Hβ contribution by assuming the typical line ratio of [O III]/Hβ from Richardson et al. (2014).

In Figure 6, the dark blue and brown dashed curves present the type II QSO and the QG+AGN templates fitted to the $z \sim 11$–17 candidates, respectively. We carry out these SED template fits at $0 < z < 20$ and obtain the best-fit redshifts at $z \sim 2$–5. Although the χ^2 values are still larger than that of the best-fit high-z galaxy solution with CIGALE (Section 3.5), all candidates, except for GHZ1/GLz11, show the type II QSO and/or QG+AGN solutions with $\Delta\chi^2$ values from the best-fit high-z galaxy solution smaller than ∼4 that is lower than the criterion generally used for the high-z galaxy candidate selection (e.g., Bowler et al. 2020; Donnan et al. 2023; Harikane et al. 2022; Finkelstein et al. 2023). Kaasinen et al. (2023) also revisited the SED fitting for HD1 with the new ALMA photometry in both 1 mm and 2 mm bands by using MAGPHYS (da Cunha et al. 2015) and obtained $\chi^2 = 2.32$ from a low-z solution at $z = 3.98$ with a QG template. These results indicate the low-z solutions can be plausible in some of the high-z candidates even with the clear NIR dropout feature and the stringent submillimeter-to-millimeter upper limits.

[51] While the sample is called Hot dust obscured galaxies (hot DOGs) in the literature, we refer it to dust reddened type I QSOs because of the clear detection of broad emission lines (Finnerty et al. 2020).

[52] In Forrest et al. (2020), we regard 10 galaxies with log(sSFR) < -1 Gyr^{-1} and [O III]+Hβ line detection as QG+AGN.

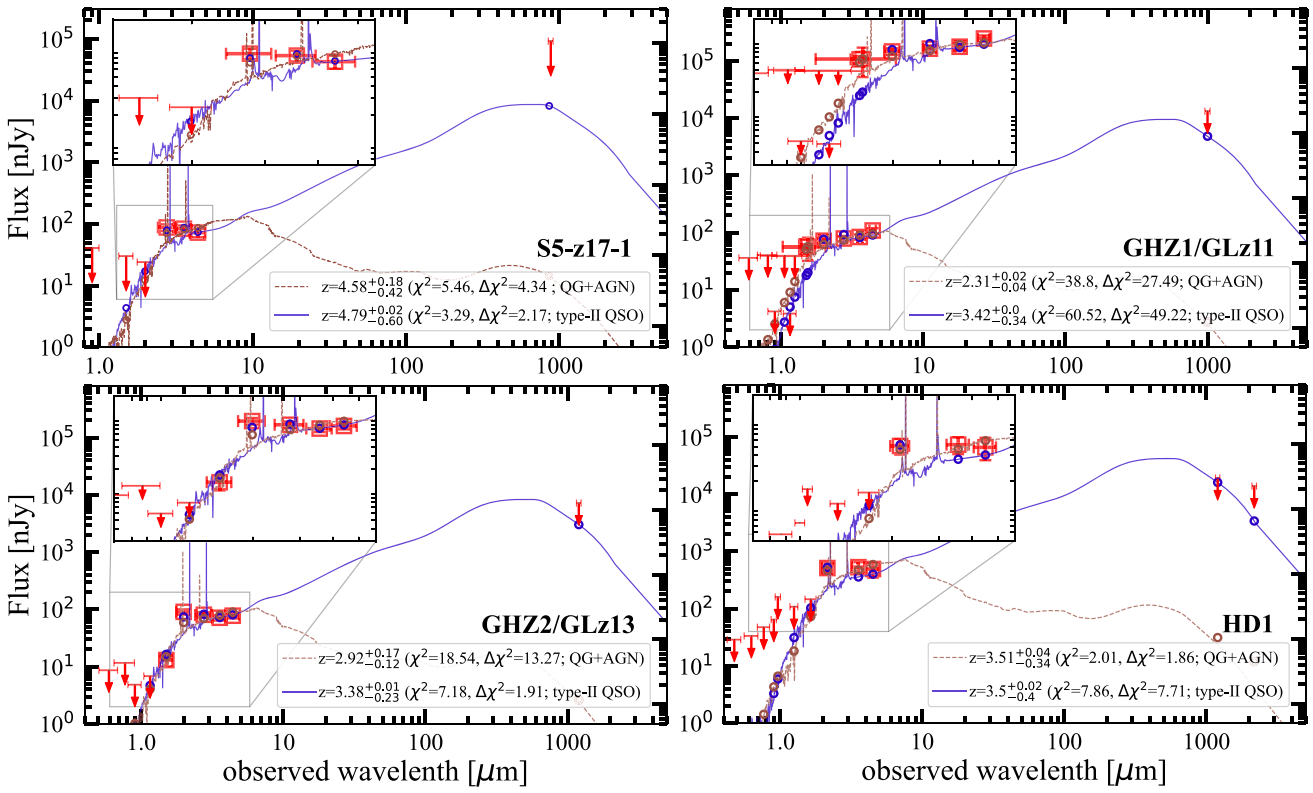

Figure 6. Same as Figure 3, but assuming QSO/AGN populations. The dark blue and brown dashed curves show the best-fit SED templates of type II QSO and QG +AGN populations, respectively, from the fitting range at $0 < z < 20$. Both templates favor the lower-z solution ($z \sim 2$–5). The $\Delta\chi^2$ value in the label indicates the difference of the χ^2 value from the best-fit high-z galaxy solution shown in Figure 3. All candidates, except for GHZ1/GLz11, have the reasonable solutions at lower-z with $\Delta\chi^2 \lesssim 4$.

5.3. Abundance

Finally, we compare the abundance of the $z \sim 11$–17 candidates with those of lower-z QG and QSO/AGN populations. Figure 7 presents the stellar mass function (SMF) for galaxies including QGs (left panel) and the LF for QSOs/AGNs (right panel) at $z \sim 3$–5 (Davidzon et al. 2017; McGreer et al. 2018; Giallongo et al. 2019; Niida et al. 2020; Onoue et al. 2023). We use the $M_{\rm star}$ and $M_{\rm UV}$ values of the $z \sim 11$–17 candidates estimated from the best-fit SEDs with CIGALE in the lower-z case at $z \sim 2$–5. To avoid the uncertainty of the dust attenuation correction, we use the observed-frame $M_{\rm UV}$ estimate. Because S5-z17-1, GHZ1/GLz11, are GHZ2/GLz13 are the most luminous high-z candidates identified in the early JWST data at each redshift, we conservatively adopt the survey area of 90.4 arcmin^2 from SMACSJ0723, GLASS, CEERS, and Stephan's Quintet fields (Harikane et al. 2023b), while we use the survey volume of 2.3 deg^2 for HD1 from (Harikane et al. 2022). We evaluate the possible redshift range Δz from the 2σ range of the $z_{\rm phot}$ estimates in the best-fit SEDs forced at $z = 2$–5, resulting in $\Delta z \sim 0.2$–0.8, depending on the candidate. We include the 1σ Poisson uncertainty presented in Gehrels (1986). Note that NIRCam medium-band filters are helpful to limit the possibility of the low-z contamination to a very narrow redshift window of $\Delta z \lesssim 0.1$ (Naidu et al. 2022a; Arrabal Haro et al. 2023a), while none of these four candidates have been observed with the medium-band filters, and it is not the case here. Another note is that the $M_{\rm UV}$ value of GHZ1/GLz11 in this forced lower-z case shows ~ -10 mag, which is located outside of the right panel, while the abundance is estimated to be $\sim 3 \times 10^{-5}$ Mpc^{-3} mag^{-1}, similar to other candidates. Such a very small $M_{\rm UV}$ value is required from the NIR dropout feature of GHZ1/GLz11 between F115W and F150W, which is the most significant by $\sim$2.9 mag among these four candidates.

In the SMF for galaxies, the green curve is drawn from the best-fit Schechter function estimated for $z \sim 3$–3.5 QGs (Davidzon et al. 2017). We find that the volume densities of GHZ1/GLz11 are much higher than the abundance of QGs by more than one order of magnitude beyond the errors. If we take the $\sim$4% into account as the possible fraction of the QG+AGN population that has strong enough emission lines among the QGs (Section 5.1), the deviation becomes even more significant (green dashed curve), and the abundances of GHZ2/GLz13 and S5-z17-1 also fall above more than one order of magnitude than that of the QG+AGN population beyond the error. This indicates that the QG+AGN population is too rare to contaminate the $z \sim 11$–17 galaxy selection in their survey volumes. On the hand, we find that the volume density of HD1 is far below the QG+AGN populations beyond the errors, suggesting that the QG+AGN population is an abundant contaminant in the survey volume of HD1. These results suggest that the possibility of contamination from the QG +AGN population is negligible in the $z \sim 11$–17 candidates, except for HD1. We note that the faint-end of the QG SMF at $z \sim 3.0$–3.5 could be rather flat, instead of the turnover shape.[53] However, the faint-end extrapolation for the QG+AGN

[53] The turnover shape is obtained at $z \sim 2.5$–3.0, which is fixed in the $z > 3$ measurements in Davidzon et al. (2017).

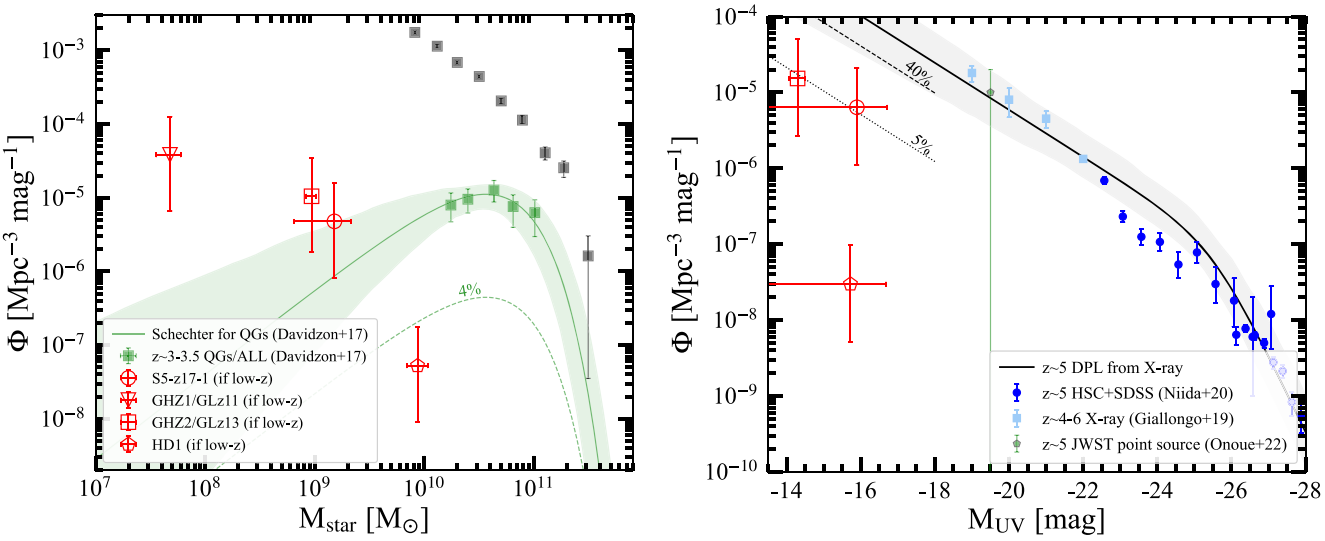

Figure 7. Left: stellar mass function (SMF) for galaxies. The red symbols represent the abundance of the $z \sim 11$–17 candidates in the case that they are the lower-z line-emitting red objects at $z \sim 2$–5. The gray and green squares show the COSMOS2015 results for entire and quiescent galaxies (QGs) at $z \sim 3$–3.5 (Davidzon et al. 2017). The green curve with the shaded region is the best-fit Schechter function with 1σ error for $z \sim 3$–3.5 QGs (Davidzon et al. 2017). Right: LF for $z \sim 4$–5 QSOs/AGNs compiled from the literature. The red symbols are the same as the left panel. The black line with the shaded region is the best-fit Double Power Law (DPL) function with 1σ error estimated for X-ray QSOs/AGNs (Giallongo et al. 2019). In both panels, the dashed curve represents the possible abundance of the QGs and the type II and/or dusty type I QSOs/AGNs with strong emission lines by scaling the QG SMF and the QSO/AGN LF by 4% and 40%, respectively, based on their EW([O III]+Hβ) distributions (Section 5.1), indicating that these populations can be abundant low-z interlopers in the survey volumes used for the identification of some of these $z \sim 11$–17 candidates. The dotted curve in the right panel shows the 5% scaling case for reference. The $M_{\rm star}$ and $M_{\rm UV}$ values are taken from the best-fit SEDs forced at $z < 8$ with CIGALE (green curves in Figure 3). GHZ1/GLz11 in this forced lower-z solution shows $M_{\rm UV} \sim -10$ mag, located outside of the figure in the right panel.

population (green dashed curve) with such a flattened shape still falls below the volume densities of S5-z17-1, GHZ1/GLz11, and GHZ2/GLz13, and thus the above argument is unchanged.

In the QSO/AGN LF, the black curve shows the best-fit Double Power Law (DPL) function from the X-ray QSO/AGN observations. Note that this is a steeper faint-end slope and a higher abundance at $M_{\rm UV} > -22$ by $\sim$1–2 orders of magnitudes than the best-fit measurement from the UV observations (e.g., Niida et al. 2020; Finkelstein & Bagley 2022). While these previous measurements are still consistent within the uncertainties, the main reason would be that the X-ray observations retrieve populations such as type II and dusty obscured QSOs/AGNs that are generally missed in the UV observations. In fact, the high fraction ($\gtrsim$80%–90%) of obscured QSOs/AGNs at $z \gtrsim 4$ have been supported from multiple aspects both from observations (e.g., Eilers et al. 2018; Vito et al. 2018; Davies et al. 2019; Morishita et al. 2020; Endsley et al. 2022; Fujimoto et al. 2022) and simulations (e.g., Ni et al. 2020; Gilli et al. 2022). We thus regard that the faint-end of the QSO/AGN LF from the X-ray observations is mostly dominated by the type II and/or dusty obscured QSOs/AGNs. It is worth mentioning that recent JWST/NIRSpec observations routinely identify broad-line AGNs and subsequently infer their abundance is close to the faint-end of the X-ray-based QSO/AGN LF (e.g., Harikane et al. 2023a; Kocevski et al. 2023).

By extrapolating the faint-end of the best-fit DPL, we find that the extrapolation exceeds the abundance of the $z \sim 11$–17 candidates by more than one order of magnitude. If we take the $\sim$40% into account as the possible fraction of the type II QSO population that has strong enough emission lines (Section 5.1), the abundance of the $z \sim 11$–17 candidates is still far below the extrapolation (black dashed curve). For reference, we find that a scaling factor of $\sim$0.05 (black dotted curve) provides the comparable abundance between the $z \sim 11$–17 candidates and the faint-end of the QSO/AGN LF. From the EW([O III]+Hβ) distribution, the fraction of the objects with minimum required EW([O III]+Hβ) of $\gtrsim$300 Å comfortably surpasses the 5% among the type II and dusty QSO/AGN populations. This indicates that the type II and/or dusty QSOs/AGNs with strong emission lines may overwhelm the abundance of the $z \sim 11$–17 candidates in the $M_{\rm UV}$ range and indeed contaminate the $z \sim 11$–17 candidates and that the secondary peak in $P(z)$ may not be negligible. For example, the middle panel of Figure 1 suggests that $P(z)$ at the secondary lower-z peak at $z \sim 5$ is $\sim$1%–20% in S5-z17-1, which may have a comparable probability if the abundance of the specific lower-z populations exceeds that of the high-z galaxies by $\sim\times$5–100. Although we first need to understand which lower-z populations are exactly the contaminants to accurately evaluate the abundance excess of such populations, these results underscore the importance of taking the high surface density of the lower-z contaminants into account in the ultra-high-redshift galaxy search.

Observations with an additional NIRCam medium-band filter limit the possibility of low-z contamination to a very narrow redshift window ($\Delta z \lesssim 0.1$; e.g., Naidu et al. 2022a). This strategy helps to mitigate the probability of low-z contaminants. However, it is worth noting that another $z \sim 17$ candidate, CEERS-93316, despite also being observed with the medium-band filter of F410M, has been spectroscopically confirmed at $z = 4.91$ (Arrabal Haro et al. 2023a). This also highlights the high surface density of the lower-z contaminants.

5.4. Remaining Low-z Possibilities

In Sections 5.1 and 5.2, we find that the subsets of QG and QSO/AGN populations actually have strong enough optical

Table 5
Remaining Low-z Possibilities from $\Delta\chi^2$ and Abundance Perspectives

Source Name	Possible Low-z Population	$z_{\rm phot}$ (χ^2)	$\Delta\chi^2$[a]	Note
S5-z17-1	Type II or dusty type I QSO/AGN	$4.79^{+0.02}_{-0.60}$ (3.29)	2.17	Very compact ($r_{\rm e} = 0\farcs05^{+0\farcs03}_{-0\farcs02}$)
	(QG+AGN)	$4.58^{+0.18}_{-0.42}$ (5.46)	4.34	Unlikely from the possible abundance
GHZ1/GLz11	...	...	...	The most secure candidate at $z \gtrsim 11$ owing to [F115W] − [F150W] > 2.9 mag
GHZ2/GLz13	Type II or dusty type I QSO/AGN	$3.38^{+0.01}_{-0.23}$ (7.18)	1.91	Very compact ($r_{\rm e} = 0\farcs02^{+0\farcs01}_{-0\farcs00}$)
HD1	QG+AGN	$3.51^{+0.04}_{-0.33}$ (2.01)	1.86	

Note.
[a] Difference of the χ^2 value from the best-fit high-z galaxy solution at $z \sim 11$–17 summarized in Table 4, suggesting that high-z solution is still favored in every candidate.

emission lines that produce reasonable SED fits ($\Delta\chi^2 \lesssim 4$) in some of the $z \sim 11$–17 candidates. In Section 5.3, we confirm that the abundance of such type II and/or dusty type I QSOs/AGNs with strong enough emission lines is higher than that of the $z \sim 11$–17 candidates, while the abundance of such QG populations is negligible, except for HD1. These results indicate the need to consider the relative surface densities of lower-z contaminants in the ultra-high-z galaxy search.

In Table 5, we summarize the remaining low-z possibilities for each candidate. If the abundance of the lower-z population is comparable or overwhelming (see Figure 7) and the low-z solution shows $\Delta\chi^2 \lesssim 4$ from the best-fit high-z solution (see Figure 6), we regard the low-z solution as the remaining possibility. This makes the QG+AGN solution in S5-z17-1 unlikely plausible because of its negligibly small abundance (Section 5.3). We find that GHZ1/GLz11 denies all lower-z solutions, showing $\Delta\chi^2 > 20$ in every type of the lower-z object we investigate in this paper. The reason for this is simply because of the fact that the most robust dropout feature is observed in GHZ1/GLz11 between the F115W and F150W filters by ∼2.9 mag (see ∼1.6–2.1 mag in the other three candidates). On the other hand, the other three sources all have the remaining low-z solutions both from $\Delta\chi^2$ and abundance perspectives, indicating that the low-z solutions cannot be ruled out in the majority of the ultra-high-z galaxy candidates.

Interestingly, we find that the possibility of the type II or dusty type I QSOs/AGNs remains in S5-z17-1 and GHZ2/GLz13 that fill the most UV luminous and compact parameter space among the recent JWST high-z candidates at $z > 9$ with $r_{\rm e} = 0\farcs02$–$0\farcs05$ (see, e.g., Figure 18 in Ono et al. 2023). While numerical simulations confirm the presence of such a compact galaxy forms at $z > 10$ (Yajima et al. 2022; see also discussion in Ono et al. 2023), the remarkably compact size might be caused by nonnegligible contribution of the emission from the QSO/AGN. This implies a very intriguing scenario of the emergence of the QSO/AGN at $z > 10$, or the lower-z interloper of the type II and/or dusty type I QSO/AGN. We also refer the reader to the discovery of a remarkably UV bright ($M_{\rm UV} \simeq -24.4$), compact, very blue ($\beta_{\rm UV} \simeq -2.2$), dust- and metal-poor starburst galaxy at $z = 2.5$ (Marques-Chaves et al. 2020), which suggests that we may be witnessing similar objects at $z \gtrsim 11$. Nevertheless, the rest-UV effective radius of the $z = 2.5$ object is measured to be $r_{\rm e} \simeq 1.2$ kpc (Marques-Chaves et al. 2020). These results suggest that S5-z17-1 and GHZ2/GLz13 are almost 10 times more compact than the $z = 2.5$ object, while the complex NIRCam point-spread function (PSF) is not yet fully characterized, and some relevant uncertainties may remain.[54] Following the recent successful spectroscopic confirmations of galaxies at $z \gtrsim 9$ with JWST/NIRSpec (e.g., Curtis-Lake et al. 2023; Roberts-Borsani et al. 2023; Williams et al. 2023; Arrabal Haro et al. 2023a, 2023b; Bunker et al. 2023; Fujimoto et al. 2023; Hsiao et al. 2023; Tang et al. 2023), confirmation of the FIR line candidate with ALMA, and/or making spectroscopic follow-up with JWST/NIRSpec, will be crucial for these UV-bright $z \sim 11$–17 candidates to reach a definitive conclusion.

6. Summary

In this paper, we present the ALMA Band 7 observations of a remarkably bright and high-redshift galaxy candidate S5-z17-1 ($M_{\rm UV} = -21.6$ at $z_{\rm phot} \sim 17$) with a robust NIRCam/F200W dropout feature identified in JWST ERO data of Stephan's Quintet. The number of UV-bright high-z candidates at $z > 9$ exceeds most pre-JWST predictions, remarking on the importance of testing lower-z contaminants, especially from populations with a red continuum and strong emission lines, which can produce similar dropout features of high-z galaxies in the NIRCam filters. In conjunction with the other three UV-bright $z \gtrsim 11$ candidates recently observed ALMA, we systematically conduct the SED analysis over the optical-to-millimeter wavelengths and discuss their physical properties in their high-z solutions and remaining low-z possibilities for each candidate. This is the first ALMA FIR census for the best candidates of remarkably UV-bright and high-redshift candidates at $z \gtrsim 11$ from the community, including the initial FIR characterization of the F200W dropout population newly identified with JWST. The main findings of this paper are summarized as follows:

1. Based on the SED analysis with the latest NIRCam photometry using CIGALE and EAZY, we confirm that a very-high-z solution of $z \geqslant 16$ is favored in S5-z17-1, while we also confirm that a red object at $z \sim 4.6$ with strong emission lines with the rest-frame equivalent width of EW([O III]+Hβ) = 450 Å produces the dropout feature between F200W and F277W filter. For plausible estimates of the surface densities of such lower-z populations, the probability of the $z \sim 4.6$ solution is comparable to the high-z solution, indicating that this source may lie at lower redshifts than originally claimed.

[54] The difference in the PSF shape has been reported between the JWST software tool `webbpsf` and the empirical approach using stars observed in the NIRCam field of view (e.g., Ding et al. 2023; Ono et al. 2023).

2. We do not detect dust continuum at 866 μm from S5-z17-1, placing the 2σ upper limit at 90.0 μJy. We adopt a spectral dust index of 2.0 and dust temperature of $T_{\rm d} = 90$ K by extrapolating the $T_{\rm d}$–z evolution model (Sommovigo et al. 2022) to $z = 18$, which is consistent of the lower limit of $T_{\rm d} > 80$ K obtained from the radiative equilibrium model (Inoue et al. 2020; Fudamoto et al. 2022) based on a clumpy ISM assumption and a very compact effective radius of $r_{\rm e} \sim 140$ pc measured in Ono et al. (2023). By assuming the single modified blackbody, we estimate the upper limit of the infrared luminosity of $L_{\rm IR} < 1.2 \times 10^{12}\,L_{\odot}$, which corresponds to SFR $< 120\,M_{\odot}$ yr^{-1}. In the case that S5-z17-1 is a lower-z object at $z \sim 4.6$, we infer $L_{\rm IR} < 2.8 \times 10^{11}\,L_{\odot}$ and SFR $< 28\,M_{\odot}$ yr^{-1}.
3. We identify a line feature with the 5.1σ level at 338.726 ± 0.007 GHz exactly at the source position. By running the blind line search algorithm of FINDCLUMP, the fidelity is estimated to be $\sim$50% in the entire data cube, suggesting that the realistic fidelity at the source position is much higher. We estimate the line width of FWHM $= 118 \pm 20$ km s^{-1} and the line intensity of $I_{\rm line} = 0.35 \pm 0.07$ Jy km s^{-1}. Based on potential redshift solutions, this line candidate is most likely either [C II] 158 μm at $z = 4.6108 \pm 0.0001$ or [O III] 52 μm at $z = 16.0089 \pm 0.0004$. Although systematic uncertainties remain in applications of empirical relations, we confirm that the SFR value inferred from the line luminosity is consistent with that estimated from the upper limit of $L_{\rm IR}$ in both cases. Either the JWST/NIRSpec and/or the ALMA 88 μm line follow-up will give a definitive conclusion as to which redshift solution is true.
4. Together with three similarly UV-bright high-redshift candidates at $z \gtrsim 11$ recently observed ALMA–GHZ1/GLz11 (Yoon et al. 2023), GHZ2/GLz13 (Bakx et al. 2023), and HD1 (Harikane et al. 2022; Kaasinen et al. 2023), we conduct the optical-to-millimeter SED analysis including the new ALMA photometry. Owing to the deep constraints from ALMA, we find that the high-z solution is strengthened in every candidate as a result of the very blue (UV continuum slope of $\beta_{\rm UV} \approx -2.3$) and luminous ($M_{\rm UV} \approx [-24: -21]$) system.
5. Based on the best-fit SEDs at $z \gtrsim 11$, we compare IRX ($\equiv L_{\rm IR}/L_{\rm UV}$), $\beta_{\rm UV}$, and $M_{\rm star}$ properties of these four candidates at $z \gtrsim 11$ with other high-z star-forming galaxies from recent ALMA studies, including the REBELS sources at $z \sim 7$ (Bouwens et al. 2022; Inami et al. 2022). We find that the $z \gtrsim 11$ candidates have generally bluer and less IR-bright properties compared to the REBELS sample, although they place a similar $M_{\rm star}$ regime and are both dominating the bright-end of the UV LF at these redshifts. This might indicate a transition taking place in the dust properties of early galaxies between $z \gtrsim 11$ and $z \sim 7$ such as the powerful dust ejection due to the radiation pressure in the very early system at $z \gtrsim 11$. We also find that HD1 explores the most massive, bluest, and IR-faintest parameter space among these high-z star-forming galaxies.
6. We also examine remaining low-z possibilities due to line-emitting red objects other than dusty star-forming galaxies. We verify type II and/or dusty type I quasars (QSOs)/AGNs and AGNs emerged in QGs based on their EW([O III]+Hβ) distributions, optical-to-millimeter SED properties, and their possible abundances. Given the survey volumes used for these $z \sim 11$–17 candidates, we find that the abundance of the QG+AGN population is negligibly small, except for HD1, while the abundance of the type II and/or dusty type I QSOs/AGNs actually overwhelms all of these candidates. We also find that the SED template of the type II QSOs and QGs including strong emission lines produces reasonable SED fits with $\Delta\chi^2 \lesssim 4$ in all candidates, except for GHZ1/GLz11 because of the most robust continuum break by $\sim$2.9 mag between F115W and F150W filters. These results suggest that lower-z possibilities are not ruled out in several of the $z \gtrsim 11$ candidates and the importance of considering the relative surface density of the lower-z contaminants in the ultra-high-z galaxy search. The detailed physical process of the dust attenuation and the ionizing background associated with the QSOs/AGNs to produce the strong emission lines with the red continuum in these potential lower-z interlopers is beyond this paper, though these topics need to be further discussed in future works.

Acknowledgments

We thank the anonymous referee for providing constructive comments and suggestions with careful review. We are grateful to Yuichi Harikane for sharing the latest photometry of S5-z17-1, helping with the comparison of the photometry, and providing useful comments on the paper. We thank Rohan Naidu, Paola Santini, Marco Castellano, Masafusa Onoue, Andrea Ferrara, Laura Sommovigo, Vasily Kokorev, Fengwu Sun, Romain Meyer, Leindert Boogaard, and Rui Marques-Chaves for helpful comments and discussions. This paper makes use of the ALMA data: ADS/JAO. ALMA #2021.A.00031.S. ALMA is a partnership of the ESO (representing its member states), NSF (USA), and NINS (Japan), together with NRC (Canada), MOST and ASIAA (Taiwan), and KASI (Republic of Korea), in cooperation with the Republic of Chile. The Joint ALMA Observatory is operated by the ESO, AUI/NRAO, and NAOJ. This work is based on observations and archival data made with the Spitzer Space Telescope, which is operated by the Jet Propulsion Laboratory, California Institute of Technology, under a contract with NASA along with archival data from the NASA/ESA Hubble Space Telescope. This research also made use of the NASA/IPAC Infrared Science Archive (IRSA), which is operated by the Jet Propulsion Laboratory, California Institute of Technology, under contract with the National Aeronautics and Space Administration. The Early Release Observations and associated materials were developed, executed, and compiled by the ERO production team: Hannah Braun, Claire Blome, Matthew Brown, Margaret Carruthers, Dan Coe, Joseph DePasquale, Nestor Espinoza, Macarena Garcia Marin, Karl Gordon, Alaina Henry, Leah Hustak, Andi James, Ann Jenkins, Anton Koekemoer, Stephanie LaMassa, David Law, Alexandra Lockwood, Amaya Moro-Martin, Susan Mullally, Alyssa Pagan, Dani Player, Klaus Pontoppidan, Charles Proffitt, Christine Pulliam, Leah Ramsay, Swara Ravindranath, Neill Reid, Massimo Robberto, Elena Sabbi, and Leonardo Ubeda. The EROs were also made possible by the foundational efforts and support from the JWST instruments, STScI planning and scheduling, and Data Management teams. This project has

received funding from the European Union's Horizon 2020 research and innovation program under the Marie Sklodowska-Curie grant agreement No. 847523 "INTERACTIONS" and from NASA through the NASA Hubble Fellowship grant No. HST-HF2-51505.001-A awarded by the Space Telescope Science Institute, which is operated by the Association of Universities for Research in Astronomy, Incorporated, under NASA contract NAS5-26555. S.F. acknowledges support from the European Research Council (ERC) Consolidator Grant funding scheme (project ConTExt, grant No. 648179). The Cosmic Dawn Center is funded by the Danish National Research Foundation under grant No. 140.

Some/all of the data presented in this paper were obtained from the Mikulski Archive for Space Telescopes (MAST) at the Space Telescope Science Institute. The specific observations analyzed can be accessed via 10.17909/6503-5145. The reduced data is also available at the University of Copenhagen Electronic Research Data archive (Brammer 2023) and on Amazon S3.[55]

Software: CASA (v6.2.1 & v6.4.1; THE CASA TEAM et al. 2022), `grizli` (Brammer et al. 2022), `eazy`, (Brammer et al. 2008), `Interferopy` (Boogaard et al. 2021), and `CIGALE` (Boquien et al. 2019).

Appendix A
JWST and HST Photmetry

In Table 6, we summarize the photometry used in our SED analysis. The photometry is evaluated with a circular aperture in $0\farcs5$ diameter and corrected to the total flux. A potential systematic uncertainty is added by 10% of the total flux in the error. For HD1, we use the optical-to-NIR photometry estimated in Harikane et al. (2022).

[55] https://s3.amazonaws.com/grizli-v2/JwstMosaics/v4/index.html

Table 6
JWST and HST Photometry Used in Our SED Analysis for $z \sim 11$–17 Candidates

ID	F606W (nJy)	F775W (nJy)	F814W (nJy)	F090W (nJy)	F105W (nJy)	F115W (nJy)	F125W (nJy)	F150W (nJy)	F160W (nJy)	F200W (nJy)	F277W (nJy)	F356W (nJy)	F444W (nJy)
S5-z17-1	⋯	⋯	⋯	8.9 ± 20.4	⋯	⋯	⋯	10.9 ± 13.2	⋯	2.4 ± 10.5	89.5 ± 11.2	84.1 ± 10.8	72.4 ± 11.4
GHZ1	-40.6 ± 18.7	⋯	-7.3 ± 20.6	2.7 ± 2.1	7.2 ± 19.9	-1.2 ± 1.9	18.6 ± 19.5	56.6 ± 6.2	57.1 ± 24.9	72.5 ± 7.6	79.1 ± 8.2	83.9 ± 8.6	108.8 ± 11.0
GHZ2	6.1 ± 4.5	1.2 ± 6.0	⋯	-0.6 ± 2.5	⋯	4.9 ± 3.5	⋯	13.1 ± 3.0	⋯	91.0 ± 9.5	80.9 ± 8.5	71.5 ± 7.5	77.7 ± 8.0

Appendix B
Possibility of CO(3–2)

In Section 3.3, we detected the FIR line at 338.726 ± 0.007 GHz at the 5.0σ level. Apart from the [C II] 158 μm at $z = 4.6$ and [O III] 52 μm at $z = 16.0$ discussed in Section 3.4, another possibility could be CO(3–2) at $z = 0.0208 \pm 0.002$, because the galaxies composed of Stephan's Quintet take the range of $z = 0.0193$–0.0225.[56] Moreover, recent NIRCam observations have identified dusty star clusters in the local galaxy of VV114, where several of them are very red in F150W − F200W, but blue in F200W − F356W (Linden et al. 2023). This implies that some specific SED shapes of the dusty star clusters might also reproduce the Lyα break. We thus also explore the CO(3–2) possibility by verifying if the SED shape of the dusty stellar clump satisfies the NIRCam color properties of S5-z17-1.

By using the dust-corrected SED of the star clusters in the local galaxy presented in Fernández-Ontiveros et al. (2009), we apply the dust extinction curves ($A_V = 1$, 5, 10, and 20) of Calzetti et al. (2000) to the SED and examine the SED shape at $\sim$1–5 μm wavelengths. We find that an SED shape similar to the Lyα break indeed appears due to the combination of the intrinsic stellar SED shape with a peak at $\sim$1.6 μm and the smaller amount of dust extinction at longer wavelengths, but the break occurs only at $\sim$1–1.5 μm, and the dropout feature between F200W and F277W cannot be reproduced. We thus conclude that the NIRCam color properties of S5-z17-1 are hard to reproduce by the local star clusters, and thus the interpretation of CO(3–2) is unlikely.

Appendix C
CIGALE Parameters for the Final Fit

In Table 7, we summarize the parameters and their boundaries used for the SED fitting with CIGALE in Section 3.

Table 7
CIGALE Modules and Input Parameters Used for All of the Fits

Parameters	Symbol	Range
Delayed SFH and recent burst		
e-folding timescale of the delayed SFH	$\tau_{\rm main}$ (Myr)	100, 250, 500, 1000
Age of the main population	Age$_{\rm main}$ (Myr)	51 log values in (1: 3.3)
Burst	$f_{\rm burst}$	No burst
SSP		
SSP		BC03
Initial mass function	IMF	Chabrier
Metallicity	Z	0.0004, 0.004, 0.02
Nebular emission		
Ionization parameter	log U	−2.0
Line width (km s^{-1})	⋯	150
Gas-phase Metallicity	zgas	0.0004, 0.004, 0.02
Electron density	ne	100
Dust attenuation law		
Color excess for both the old and young stellar populations	E_BV_lines	21 log values in (−3: 1.3)
Reduction factor to apply on E_BV_lines to compute $E(B-V)$ s the stellar continuum attenuation	E_BV_factor	1.0
Bump amplitude	uv_bump_amplitude	0.0
Power-law slope	power law_slope	0.0
Extinction law to use for attenuating the emission lines flux	Ext_law_emission_lines	SMC
Ratio of total to selective extinction, $A_V/E(B-V)$	Rv	3.1
Dust emission (DL2014)		
Mass fraction of polycyclic aromatic hydrocarbons	$q_{\rm PAH}$	0.47
Minimum radiation field	$U_{\rm min}$	5.0
Power-law slope $dU/dM \approx U^{\alpha}$	$-\alpha$	2.0
Dust fraction in photodissociation regions	γ	0.1
No AGN emission		

Note. BC03 indicates Bruzual & Charlot (2003), and the Chabrier IMF refers to Chabrier (2003).

[56] http://ned.ipac.caltech.edu/

Appendix D
Fidelity of Line

We investigate the fidelity of the line detection at 338.726 ± 0.007 GHz by using a blind line search algorithm of FINDCLUMP. Figure 8 summarizes the fidelity as a function of SNR of the 3D clump evaluated with FINDCLUMP. We find the excess in the positive histogram at SNR > 5.0, which assures the line detection of 338.726 ± 0.007 GHz. Although the fidelity curve suggests that the fidelity at SNR $= 5.1$ is $\sim$50%, we emphasize that this is a blind search in the full data cube. Given no spatial offsets of the line and the target source, the realistic fidelity increases much higher than 50%.

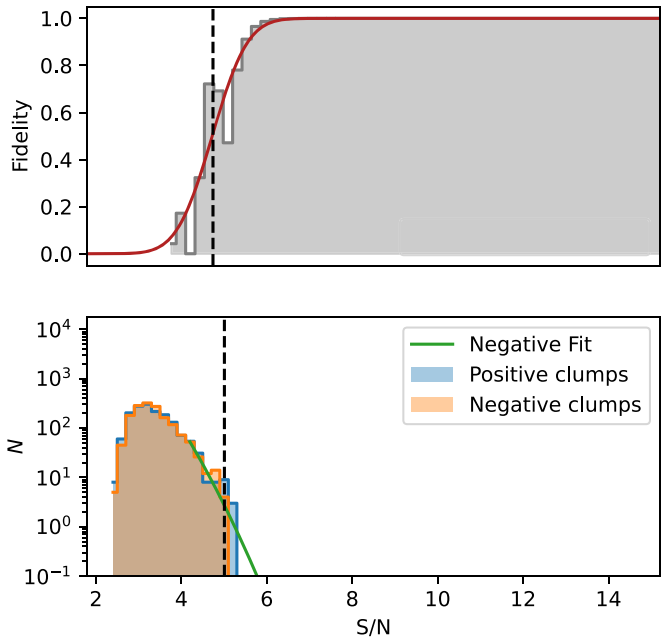

Figure 8. Fidelity of the 3D clumps as a function of S/N produced by a blind line search algorithm FINDCLUMP in our ALMA Band 7 data cube for S5-z17-1. Here we show the results with the 15 km width data cube smoothed with the six-channel kernel, where the line candidate is identified with FINDCLUMP at the 5σ level. Bottom: histograms of positive and negative clumps. Top: fidelity estimated from the histograms of positive and negative clumps as a function of S/N. The dashed line corresponds to the $\sim$338.7 GHz line feature exactly at the source position, indicating that the fidelity is $\sim$50%. Note that this is a blind search in the entire cube. Based on the survey volume only around the central target, the realistic fidelity should be much higher than 50%.

ORCID iDs

Seiji Fujimoto https://orcid.org/0000-0001-7201-5066
Steven L. Finkelstein https://orcid.org/0000-0001-8519-1130
Denis Burgarella https://orcid.org/0000-0002-4193-2539
Chris L. Carilli https://orcid.org/0000-0001-6647-3861
Véronique Buat https://orcid.org/0000-0003-3441-903X
Caitlin M. Casey https://orcid.org/0000-0002-0930-6466
Laure Ciesla https://orcid.org/0000-0003-0541-2891
Sandro Tacchella https://orcid.org/0000-0002-8224-4505
Jorge A. Zavala https://orcid.org/0000-0002-7051-1100
Gabriel Brammer https://orcid.org/0000-0003-2680-005X
Yoshinobu Fudamoto https://orcid.org/0000-0001-7440-8832
Masami Ouchi https://orcid.org/0000-0002-1049-6658
Francesco Valentino https://orcid.org/0000-0001-6477-4011
M. C. Cooper https://orcid.org/0000-0003-1371-6019
Mark Dickinson https://orcid.org/0000-0001-5414-5131
Maximilien Franco https://orcid.org/0000-0002-3560-8599
Mauro Giavalisco https://orcid.org/0000-0002-7831-8751
Taylor A. Hutchison https://orcid.org/0000-0001-6251-4988
Jeyhan S. Kartaltepe https://orcid.org/0000-0001-9187-3605
Anton M. Koekemoer https://orcid.org/0000-0002-6610-2048
Takashi Kojima https://orcid.org/0000-0001-5780-1886
Rebecca L. Larson https://orcid.org/0000-0003-2366-8858
E. J. Murphy https://orcid.org/0000-0001-7089-7325
Casey Papovich https://orcid.org/0000-0001-7503-8482
Pablo G. Pérez-González https://orcid.org/0000-0003-4528-5639
Rachel S. Somerville https://orcid.org/0000-0002-6748-6821
Ilsang Yoon https://orcid.org/0000-0001-9163-0064
Stephen M. Wilkins https://orcid.org/0000-0003-3903-6935
Hollis Akins https://orcid.org/0000-0003-3596-8794
Ricardo O. Amorín https://orcid.org/0000-0001-5758-1000
Pablo Arrabal Haro https://orcid.org/0000-0002-7959-8783
Micaela B. Bagley https://orcid.org/0000-0002-9921-9218
Katherine Chworowsky https://orcid.org/0000-0003-4922-0613
Nikko J. Cleri https://orcid.org/0000-0001-7151-009X
Olivia R. Cooper https://orcid.org/0000-0003-3881-1397
Luca Costantin https://orcid.org/0000-0001-6820-0015
Emanuele Daddi https://orcid.org/0000-0002-3331-9590
Henry C. Ferguson https://orcid.org/0000-0001-7113-2738
Norman A. Grogin https://orcid.org/0000-0001-9440-8872
E. F. Jiménez-Andrade https://orcid.org/0000-0002-2640-5917
Stéphanie Juneau https://orcid.org/0000-0002-0000-2394
Allison Kirkpatrick https://orcid.org/0000-0002-5537-8110
Dale D. Kocevski https://orcid.org/0000-0002-8360-3880
Aurélien Le Bail https://orcid.org/0000-0002-9466-2763
Arianna Long https://orcid.org/0000-0002-7530-8857
Ray A. Lucas https://orcid.org/0000-0003-1581-7825
Benjamin Magnelli https://orcid.org/0000-0002-6777-6490
Jed McKinney https://orcid.org/0000-0002-6149-8178
Caitlin Rose https://orcid.org/0000-0002-8018-3219
Lise-Marie Seillé https://orcid.org/0000-0001-7755-4755
Raymond C. Simons https://orcid.org/0000-0002-6386-7299
Benjamin J. Weiner https://orcid.org/0000-0001-6065-7483
L. Y. Aaron Yung https://orcid.org/0000-0003-3466-035X

References

Adams, N. J., Conselice, C. J., Ferreira, L., et al. 2023, MNRAS, 518, 4755
Arrabal Haro, P., Dickinson, M., Finkelstein, S. L., et al. 2023a, arXiv:2303.15431
Arrabal Haro, P., Dickinson, M., Finkelstein, S. L., et al. 2023b, ApJL, 951, L22
Atek, H., Shuntov, M., Furtak, L. J., et al. 2023, MNRAS, 519, 1201
Bakx, T. J. L. C., Zavala, J. A., Mitsuhashi, I., et al. 2023, MNRAS, 519, 5076
Barrufet, L., Oesch, P. A., Weibel, A., et al. 2023, MNRAS, 522, 449
Behroozi, P., Conroy, C., Wechsler, R. H., et al. 2020, MNRAS, 499, 5702
Belli, S., Genzel, R., Förster Schreiber, N. M., et al. 2017a, ApJL, 841, L6
Belli, S., Newman, A. B., & Ellis, R. S. 2017b, ApJ, 834, 18
Belli, S., Newman, A. B., & Ellis, R. S. 2019, ApJ, 874, 17

Boogaard, L., Meyer, R. A., & Novak, M. 2021a, Interferopy: Analysing Datacubes from Radio-to-submm Observations, Zenodo, doi:10.5281/ZENODO.5775603
Boquien, M., Burgarella, D., Roehlly, Y., et al. 2019, A&A, 622, A103
Bouwens, R., González-López, J., Aravena, M., et al. 2020, ApJ, 902, 112
Bouwens, R. J., Smit, R., Schouws, S., et al. 2022, ApJ, 931, 160
Bouwens, R. J., Stefanon, M., Brammer, G., et al. 2023, MNRAS, 523, 1036
Bowler, R. A. A., Dunlop, J. S., McLure, R. J., et al. 2014, MNRAS, 440, 2810
Bowler, R. A. A., Jarvis, M. J., Dunlop, J. S., et al. 2020, MNRAS, 493, 2059
Boyer, M. L., Anderson, J., Gennaro, M., et al. 2022, RNAAS, 6, 191
Boylan-Kolchin, M. 2023, NatAs, 7, 731
Bradley, L. D., Coe, D., Brammer, G., et al. 2023, ApJ, 955, 13
Brammer, G. 2023, JWST Image Mosaics grizli-v4, University of Copenhagen, v1.8.3, Zenodo, doi: 10.5281/zenodo.7767790
Brammer, G., & Matharu, J. 2021, gbrammer/grizli: Release 2021, v1.3.2, Zenodo, doi:10.5281/zenodo.5012699
Brammer, G., Strait, V., Matharu, J., & Momcheva, I. 2022, grizli, v1.5.0, Zenodo, doi:10.5281/zenodo.6672538
Brammer, G. B., van Dokkum, P. G., & Coppi, P. 2008, ApJ, 686, 1503
Bruzual, G., & Charlot, S. 2003, MNRAS, 344, 1000
Bunker, A. J., Saxena, A., Cameron, A. J., et al. 2023, A&A, 677, A88
Burgarella, D., Bogdanoska, J., Nanni, A., et al. 2022, A&A, 664, A73
Burgarella, D., Buat, V., & Iglesias-Páramo, J. 2005, MNRAS, 360, 1413
Calzetti, D., Armus, L., Bohlin, R. C., et al. 2000, ApJ, 533, 682
Carilli, C. L., & Walter, F. 2013, ARA&A, 51, 105
Castellano, M., Fontana, A., Treu, T., et al. 2022, ApJL, 938, L15
Chabrier, G. 2003, PASP, 115, 763
Conroy, C., & Gunn, J. E. 2010, ApJ, 712, 833
Conroy, C., Gunn, J. E., & White, M. 2009, ApJ, 699, 486
Curtis-Lake, E., Carniani, S., Cameron, A., et al. 2023, NatAs, 7, 622
da Cunha, E., Groves, B., Walter, F., et al. 2013, ApJ, 766, 13
da Cunha, E., Walter, F., Smail, I. R., et al. 2015, ApJ, 806, 110
Davidzon, I., Ilbert, O., Laigle, C., et al. 2017, A&A, 605, A70
Davies, F. B., Hennawi, J. F., & Eilers, A.-C. 2019, ApJL, 884, L19
De Looze, I., Cormier, D., Lebouteiller, V., et al. 2014, A&A, 568, A62
Dessauges-Zavadsky, M., Ginolfi, M., Pozzi, F., et al. 2020, A&A, 643, A5
Díaz-Santos, T., Armus, L., Charmandaris, V., et al. 2013, ApJ, 774, 68
Ding, X., Onoue, M., Silverman, J. D., et al. 2023, Natur, 621, 7977
Donnan, C. T., McLeod, D. J., Dunlop, J. S., et al. 2023, MNRAS, 518, 6011
Draine, B. T., Aniano, G., Krause, O., et al. 2014, ApJ, 780, 172
Eilers, A.-C., Hennawi, J. F., & Davies, F. B. 2018, ApJ, 867, 30
Endsley, R., Stark, D. P., Charlot, S., et al. 2021, MNRAS, 502, 6044
Endsley, R., Stark, D. P., Fan, X., et al. 2022, MNRAS, 512, 4248
Fernández-Ontiveros, J. A., Prieto, M. A., & Acosta-Pulido, J. A. 2009, MNRAS, 392, L16
Ferrara, A., Pallottini, A., & Dayal, P. 2023, MNRAS, 522, 3986
Finkelstein, S. L., & Bagley, M. B. 2022, ApJ, 938, 25
Finkelstein, S. L., Bagley, M. B., Ferguson, H. C., et al. 2023, ApJL, 946, L13
Finkelstein, S. L., Bagley, M. B., Haro, P. A., et al. 2022, ApJL, 940, L55
Finkelstein, S. L., Song, M., Behroozi, P., et al. 2015, ApJ, 814, 95
Finnerty, L., Larson, K., Soifer, B. T., et al. 2020, ApJ, 905, 16
Forrest, B., Marsan, Z. C., Annunziatella, M., et al. 2020, ApJ, 903, 47
Franco, M., Elbaz, D., Béthermin, M., et al. 2018, A&A, 620, A152
Fudamoto, Y., Inoue, A. K., & Sugahara, Y. 2023, MNRAS, 521, 2962
Fudamoto, Y., Inoue, A. K., & Sugahara, Y. 2022, ApJL, 938, L24
Fudamoto, Y., Oesch, P. A., Faisst, A., et al. 2020, A&A, 643, A4
Fudamoto, Y., Oesch, P. A., Schouws, S., et al. 2021, Natur, 597, 489
Fujimoto, S., Arrabal Haro, P., Dickinson, M., et al. 2023, ApJL, 949, L25
Fujimoto, S., Brammer, G. B., Watson, D., et al. 2022, Natur, 604, 261
Fujimoto, S., Oguri, M., Brammer, G., et al. 2021, ApJ, 911, 99
Fujimoto, S., Ouchi, M., Ferrara, A., et al. 2019, ApJ, 887, 107
Fujimoto, S., Ouchi, M., Ono, Y., et al. 2016, ApJS, 222, 1
Fujimoto, S., Silverman, J. D., Bethermin, M., et al. 2020, ApJ, 900, 1
Fukushima, H., & Yajima, H. 2021, MNRAS, 506, 5512
Fukushima, H., Yajima, H., Sugimura, K., et al. 2020, MNRAS, 497, 3830
Gaia Collaboration, Brown, A. G. A., Vallenari, A., et al. 2021, A&A, 649, A1
Gehrels, N. 1986, ApJ, 303, 336
Giallongo, E., Grazian, A., Fiore, F., et al. 2019, ApJ, 884, 19
Gilli, R., Norman, C., Calura, F., et al. 2022, A&A, 666, A17
Gullberg, B., De Breuck, C., Vieira, J. D., et al. 2015, MNRAS, 449, 2883
Harikane, Y., Inoue, A. K., Mawatari, K., et al. 2022, ApJ, 929, 1
Harikane, Y., Nakajima, K., Ouchi, M., et al. 2023a, arXiv:2304.06658
Harikane, Y., Ouchi, M., Oguri, M., et al. 2023b, ApJS, 265, 5
Hsiao, T. Y.-Y., Abdurro'uf, Coe, D., et al. 2023, arXiv:2305.03042
Inami, H., Algera, H. S. B., Schouws, S., et al. 2022, MNRAS, 515, 3126
Inayoshi, K., Harikane, Y., Inoue, A. K., Li, W., & Ho, L. C. 2022, ApJL, 938, L10
Inoue, A. K., Hashimoto, T., Chihara, H., & Koike, C. 2020, MNRAS, 495, 1577
Ito, K., Tanaka, M., Miyaji, T., et al. 2022, ApJ, 929, 53
Jiang, L., Kashikawa, N., Wang, S., et al. 2021, NatAs, 5, 256
Johnson, B. D., Leja, J., Conroy, C., & Speagle, J. S. 2021, ApJS, 254, 22
Jones, G. C., Béthermin, M., Fudamoto, Y., et al. 2020, MNRAS, 491, L18
Kaasinen, M., van Marrewijk, J., Popping, G., et al. 2023, A&A, 671, A29
Kennicutt, R. C., Jr. 1998, ApJ, 498, 541
Kim, J.-G., Kim, W.-T., & Ostriker, E. C. 2018, ApJ, 859, 68
Kocevski, D. D., Onoue, M., Inayoshi, K., et al. 2023, ApJL, 954, L4
Kokorev, V., Brammer, G., Fujimoto, S., et al. 2022, ApJS, 263, 38
Krumholz, M. R., McKee, C. F., & Bland-Hawthorn, J. 2019, ARA&A, 57, 227
Kubo, M., Umehata, H., Matsuda, Y., et al. 2022, ApJ, 935, 89
Labbé, I., Oesch, P. A., Bouwens, R. J., et al. 2013, ApJL, 777, L19
Labbe, I., van Dokkum, P., Nelson, E., et al. 2023, Natur, 616, 266
Lagache, G., Cousin, M., & Chatzikos, M. 2018, A&A, 609, A130
Le Fèvre, O., Béthermin, M., Faisst, A., et al. 2020, A&A, 643, A1
Linden, S. T., Evans, A. S., Armus, L., et al. 2023, ApJL, 944, L55
Lovell, C. C., Harrison, I., Harikane, Y., Tacchella, S., & Wilkins, S. M. 2023, MNRAS, 518, 2511
Marques-Chaves, R., Álvarez-Márquez, J., Colina, L., et al. 2020, MNRAS, 499, L105
Mason, C. A., Trenti, M., & Treu, T. 2023, MNRAS, 521, 497
McGreer, I. D., Fan, X., Jiang, L., & Cai, Z. 2018, AJ, 155, 131
McKinney, J., Finnerty, L., Casey, C. M., et al. 2023, ApJL, 946, L39
Menci, N., Castellano, M., Santini, P., et al. 2022, ApJL, 938, L5
Morishita, T., & Stiavelli, M. 2023, ApJL, 946, L35
Morishita, T., Stiavelli, M., Trenti, M., et al. 2020, ApJ, 904, 50
Naidu, R. P., Oesch, P. A., Setton, D. J., et al. 2022a, arXiv:2208.02794
Naidu, R. P., Oesch, P. A., van Dokkum, P., et al. 2022b, ApJL, 940, L14
Nanayakkara, T., Glazebrook, K., Jacobs, C., et al. 2023, AJ, 947, L26
Nardiello, D., Bedin, L. R., Burgasser, A., et al. 2022, MNRAS, 517, 484
Ni, Y., Di Matteo, T., Gilli, R., et al. 2020, MNRAS, 495, 2135
Niida, M., Nagao, T., Ikeda, H., et al. 2020, ApJ, 904, 89
Noll, S., Burgarella, D., Giovannoli, E., et al. 2009, A&A, 507, 1793
Oesch, P. A., Brammer, G., van Dokkum, P. G., et al. 2016, ApJ, 819, 129
Ono, Y., Harikane, Y., Ouchi, M., et al. 2023, ApJ, 951, 72
Onoue, M., Inayoshi, K., Ding, X., et al. 2023, ApJL, 942, L17
Pallottini, A., Gallerani, S., Ferrara, A., et al. 2015, MNRAS, 453, 1898
Peeters, E., Martín-Hernández, N. L., Damour, F., et al. 2002, A&A, 381, 571
Pei, Y. C. 1992, ApJ, 395, 130
Pérez-González, P. G., Barro, G., Annunziatella, M., et al. 2023, ApJL, 951, L1
Polletta, M., Tajer, M., Maraschi, L., et al. 2007, ApJ, 663, 81
Polletta, M. d. C., Wilkes, B. J., Siana, B., et al. 2006, ApJ, 642, 673
Pontoppidan, K., Blome, C., Braun, H., et al. 2022, ApJL, 936, L14
Popping, G. 2023, A&A, 669, L8
Richardson, C. T., Allen, J. T., Baldwin, J. A., Hewett, P. C., & Ferland, G. J. 2014, MNRAS, 437, 2376
Roberts-Borsani, G., Treu, T., Chen, W., et al. 2023, Natur, 618, 480
Roberts-Borsani, G. W., Bouwens, R. J., Oesch, P. A., et al. 2016, ApJ, 823, 143
Rodighiero, G., Bisigello, L., Iani, E., et al. 2023, MNRAS, 518, L19
Romano, M., Cassata, P., Morselli, L., et al. 2020, MNRAS, 496, 875
Smit, R., Bouwens, R. J., Franx, M., et al. 2015, ApJ, 801, 122
Smit, R., Bouwens, R. J., Labbé, I., et al. 2014, ApJ, 784, 58
Sommovigo, L., Ferrara, A., Pallottini, A., et al. 2022, MNRAS, 513, 3122
Stefanon, M., Bouwens, R. J., Labbé, I., et al. 2021, ApJ, 922, 29
Steinhardt, C. L., Capak, P., Masters, D., & Speagle, J. S. 2016, ApJ, 824, 21
Steinhardt, C. L., Kokorev, V., Rusakov, V., Garcia, E., & Sneppen, A. 2023, ApJL, 951, L40
Sun, F., Egami, E., Pérez-González, P. G., et al. 2021, ApJ, 922, 114
Tacchella, S., Bose, S., Conroy, C., Eisenstein, D. J., & Johnson, B. D. 2018, ApJ, 868, 92
Tacconi, L. J., Neri, R., Genzel, R., et al. 2013, ApJ, 768, 74
Tang, M., Stark, D. P., Chen, Z., et al. 2023, MNRAS, in press
THE CASA TEAM, Bean, B., Bhatnagar, S., et al. 2022, PASP, 134, 114501
Treu, T., Roberts-Borsani, G., Bradac, M., et al. 2022, ApJ, 935, 110
Vito, F., Brandt, W. N., Yang, G., et al. 2018, MNRAS, 473, 2378
Walter, F., Decarli, R., Aravena, M., et al. 2016, ApJ, 833, 67
Wang, R., Wagg, J., Carilli, C. L., et al. 2013, ApJ, 773, 44
Wang, T., Schreiber, C., Elbaz, D., et al. 2019, Natur, 572, 211
Williams, C. C., Labbe, I., Spilker, J., et al. 2019, ApJ, 884, 154
Williams, H., Kelly, P. L., Chen, W., et al. 2023, Sci, 380, 416

Yajima, H., Abe, M., Khochfar, S., et al. 2022, MNRAS, 509, 4037
Yamaguchi, Y., Kohno, K., Hatsukade, B., et al. 2019, ApJ, 878, 73
Yan, H., Ma, Z., Ling, C., et al. 2023, ApJL, 942, L9
Yang, L., Morishita, T., Leethochawalit, N., et al. 2022, ApJL, 938, L17
Yang, S., Lidz, A., & Popping, G. 2021, MNRAS, 504, 723
Yoon, I., Carilli, C. L., Fujimoto, S., et al. 2023, ApJ, 950, 61
Zakamska, N. L., Strauss, M. A., Krolik, J. H., et al. 2003, AJ, 126, 2125
Zavala, J. A., Buat, V., Casey, C. M., et al. 2023, ApJL, 943, L9
Zhang, Z.-Y., Papadopoulos, P. P., Ivison, R. J., et al. 2016, RSOS, 3, 160025
Zhou, L., Elbaz, D., Franco, M., et al. 2020, A&A, 642, A155
Ziparo, F., Ferrara, A., Sommovigo, L., & Kohandel, M. 2023, MNRAS, 520, 2445